PART I

Time-Integrated Synchrotron-Radiation Spectroscopy

A new technique for nuclear resonant forward scattering of synchrotron radiation

Chapter 1

Introduction to Nuclear Resonant Scattering of Synchrotron Radiation

A nucleus embedded in a solid state will be submitted to so-called hyperfine interactions which will split the nuclear levels into several sublevels. The two most important hyperfine interactions are the electrical quadrupole and the magnetic dipole interaction. The former describes the interaction of the nuclear quadrupole moment (this is essentially a measure for the deformation from sphericity of the nuclear charge distribution) with the electrical field gradient, originating from a non-cubic symmetric charge distribution at the nuclear site. The magnetic dipole interaction describes the coupling of the nuclear magnetic moment to the magnetic fields. It is not the scope of this text to explain hyperfine interactions in detail. For that, we refer to the many textbooks on this subject.
Measurements of hyperfine interactions generally give information either on the nuclear moments or on the fields at the position of the nucleus.

Many different hyperfine interaction techniques have been developed, which are nicely reviewed by Schatz [1]. The most widely used method is without any doubt Mössbauer spectroscopy. It dates back to 1958 when Mössbauer discovered the possibility of recoilless emission and absorption of γ-rays by nuclei, known as the Mössbauer effect [2, 3]. The most remarkable property of Mössbauer spectroscopy is its outstanding energy resolution. In case of the 14.413 keV transition of ^{57}Fe, e.g., a resolution of $3 \cdot 10^{-13}$ is achieved. This low value, defined by the ratio of the nuclear excited level width Γ and the transition energy E_0, allows to measure hyperfine splittings in nuclei.

For example, the splitting at room temperature of the first excited state in $\alpha-^{57}$Fe due to the magnetic dipole interaction is typically 108 neV or $7 \cdot 10^{-12}$ times the transition energy. Using the Doppler shift, one can bring source and absorber nuclei in resonance (even if they are subjected to different hyperfine interactions) by simply moving the source relative to the absorber. In most cases, velocities in the order of a few mm/s are sufficient. (More information on Mössbauer spectroscopy can be found, e.g., in Ref. [4].)
The determination of the energy dependence of the nuclear cross-section by means of velocity spectra has become the standard method for Mössbauer spectroscopy and found its application in different branches of science, such as physics, chemistry, biology, ... Most of these experiments, however, only use the energy dependence of the cross-section. Time dependence and polarization characteristics of the nuclear transition are not exploited.

In 1974 Ruby suggested to use synchrotron radiation for nuclear resonance experiments [5]. Synchrotron radiation has some unique features such as a pulsed time structure and a high degree of polarization, which allow experiments that are complementary to classical Mössbauer spectroscopy. Since 1975 strong efforts have been made to combine the attractive properties of synchrotron radiation with the excellent energy resolution of the Mössbauer effect. Nevertheless, it lasted until 1985 before the first successful experiment was performed by Gerdau [6]. Nuclear resonant scattering of synchrotron radiation was observed on an yttrium iron garnet (YIG) crystal, highly enriched in ^{57}Fe. Soon after the first observation, the time resolution was improved, and quantum beats in the time spectrum were revealed, which are the fingerprints of the hyperfine splittings [7, 8].

Since that pioneering work, many nuclear resonance fluorescence experiments have followed (see the reviews by Gerdau et al. [9], Arthur et al. [10], Rüffer [11], Gerdau and van Bürck [12] and Smirnov [13]). The early experiments suffered from very low count rates. This problem was solved by the advent of third generation synchrotrons. Hard synchrotron radiation (in the X-ray range) is generated at the new sources by undulators. The angular flux density of the generated resonant radiation far exceeds that of a Mössbauer source. For example, a 20 mCi ^{57}Co source produces a 14.413 keV radiation intensity of about 10^4 quanta per second into the solid angle $3^\circ \times 3^\circ$. An undulator at a third generation synchrotron produces approximately the same intensity of 14.413 keV quanta but within a 10^6 times smaller solid angle. Moreover, the synchrotron beam is nearly 100% linearly polarized. These unique properties made nuclear resonant scattering with synchrotron radiation very attractive and dedicated beamlines were commissioned at third generation synchrotrons. In 1994, a nuclear resonant scattering beamline became available at the European Synchrotron Radiation Facility (ESRF) in Grenoble (France), followed by one at the Advanced Photon Source (APS) at Argonne (U.S.A.) in 1996, and at the new

synchrotron facility SPring-8 in Harima Science Garden City (Japan) in 1998. In addition, there are dedicated beamlines at Hamburg Synchrotron Radiation Laboratory (HASYLAB) in Germany and at the National Synchrotron Light Source (NSLA) in Brookhaven (U.S.A.).
Today, the field of nuclear resonant scattering of synchrotron radiation comprises Bragg and Laue reflections by single crystals and multilayers, total external reflection and nuclear forward scattering to which this work is devoted.

In this introductory chapter, the properties of synchrotron radiation are discussed.
One section is devoted to time differential synchrotron-radiation spectroscopy, the common technique for nuclear scattering experiments with synchrotron radiation. This method, that has proved to be successful, has some shortcomings and disadvantages which will be pointed out.
In the third section, we describe a recently developed time-integrated technique which does not suffer from the problems of the time differential measurements. This will be the subject of the thesis. A short explanation on the new method is given; a more profound treatment follows in the next chapters.

1.1 Properties of Synchrotron Radiation

1. High Brilliance

As already mentioned, synchrotron radiation is characterized by very high intensities and small beam divergence. This makes it a very attractive radiation source.

2. Pulsed Time Structure

Synchrotron radiation is generated by charged particles that are kept in a closed orbit. The electrons that orbit the synchrotron storage ring are tightly packed in bunches. When the charged particles pass by a bending magnet or some periodic magnetic structure such as an undulator, they produce discrete pulses of radiation which last for about 100 ps. The interval between the pulses depends on the filling mode. The maximum number of electron bunches in the storage ring is determined by the circumference and rf acceleration frequency. For APS this gives 1296 synchrotron pulses with a separation of 2.84 ns. However, the storage ring can be partially filled, yielding intervals between pulses equal to several times 2.8 ns. The maximum interval is 3.68 μs, the period of orbit of one electron bunch. In reality, though, the time between successive pulses is always less. Intervals of 1 μs are already very exceptional. In Ref. [14] the timing parameters for several synchrotron radiation sources can be found.

3. Linear Polarization

Synchrotron Radiation is for 96% linearly polarized in the plane of the storage ring. This is shown in figure 1.1.

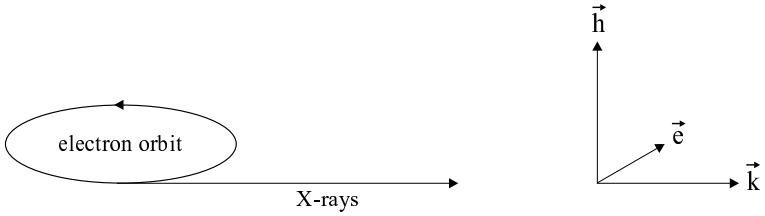

Figure 1.1: Polarization of synchrotron radiation, given by $\vec{e}^{\,\sigma}$ and $\vec{h}^{\sigma}$, the electric and magnetic polarization vectors for a σ-polarized electromagnetic wave.

4. Small Beam Size

The unfocused beam spot at 30 m from the undulator is typically 1.0×0.8 mm^2 (FWHM). This, together with the small beam divergence, allows experiments on very small samples.

5. Broad Energy Spectrum

The radiation emitted by a bending magnet has a spectral band width of several 100 keV. An undulator produces radiation which is peaked around one particular energy. But still, the total band extends over several keV. An interesting feature is that the undulator can be tuned to a particular energy.

Table 1.1 summarizes the properties of synchrotron radiation and compares them to γ-radiation from a Mössbauer source.

Table 1.1: Comparison between synchrotron radiation and radiation produced by a Mössbauer source.

Properties of emitted radiation	synchrotron source	Mössbauer source
spectrum	broadband tunable	monochromatic
polarization	linear	none
time structure	pulsed	continuous
intensity	very high	relatively low
directionality	emission in very small cone	isotropic emission

1.2 Time Differential Synchrotron-Radiation Spectroscopy (TDSRS)

Nuclear resonance scattering experiments with synchrotron radiation are generally performed in a time differential mode, in which the nuclear decay is studied as a function of time after excitation by the synchrotron pulse.

If one considers resonant scattering of a γ-ray by an individual nucleus, the scattered intensity as a function of time will show an exponential decay, determined by the lifetime of the nuclear excited state. In case of an ensemble of resonant nuclei there will be spatial coherence between the different scattering paths and the decay will be modulated by multiple scattering of the radiation.
At resonance, each nuclear scattering in forward direction introduces a phase shift of 180°. Most radiation will be scattered only once. In thicker absorbers, however, there is a certain probability for double scattering with an additional phase shift of 180°. The single-scattered radiation and the double-scattered radiation are in antiphase, yielding a negative interference. Due to this destructive interference, the decay probability of the nuclear ensemble is decreased and the scattered intensity is lower than in the case of isolated nuclei. Historically, this phenomenon has been called 'speedup' because the decay seem to go faster than exponential.
In thick samples, there is also a certain probability for triple scattering, which is again in-phase with the single scattering, and hence interferes constructively with it. For small times, the chance for multiple scattering is very low due to the lifetime of the excited state. As time elapses, the probability for double-scattering events increases and a destructive interference is observed in the time spectra by a decrease of intensity. For even larger times, triple scattering comes up and a positive interference will yield an increase of intensity, etc. A dynamical beat pattern is created. The period between subsequent maxima and minima is non-equidistant and decreases as the sample thickness increases. The interpretation of the speedup and dynamical beats in terms of multiple scattering events follows from the quantum mechanical theory of Hoy [15].

When synchrotron radiation is used to excite nuclei, another coherence effect arises. Since the incident radiation has a broadband energy spectrum, all hyperfine levels can be excited at once, giving rise to interferences between the different nuclear transitions for which the scattered photons have the same polarization. This so-called energy coherence can occur between hyperfine transitions within a single nucleus (intra-nuclear coherence), but also between the transitions of different nuclei (inter-nuclear coherence).

For instance, if a sample contains two subsets of nuclei in a different chemical environment so that there is an isomer shift in the transition energy of one subset with respect to the other subset, then synchrotron radiation can excite nuclei in both sets, resulting again in interference of the scattered radiation. The interference shows up as fast quantum beats in the time spectrum, which are superposed on the exponential (or speeded-up) decay [16]. The oscillation frequency depends on the energy difference between the possible nuclear transitions. An accurate determination of the beat frequency provides very precise information on the hyperfine interaction parameters [17].

To conclude, a TDSRS spectrum will show three features. The time behavior of scattering by a nuclear ensemble is essentially exponential with an increased decay rate (speedup). In addition, the time spectrum will be modulated by a slowly varying envelope (dynamical beats) due to multiple scattering, and by fast quantum beats originating from energy differences between nuclear transitions.
Figure 1.2 shows a typical TDSRS spectrum. The three characteristics are easily recognized. Note that the ordinate is logarithmic. The dashed line gives a pure exponential decay (from a single nucleus).

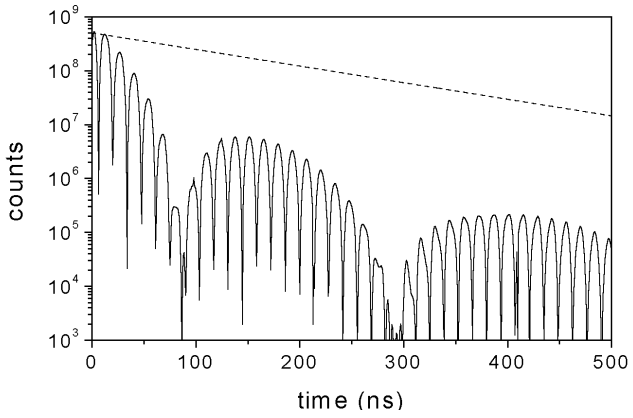

Figure 1.2: Simulation of the TDSRS spectrum from a ^{57}Fe absorber with effective thickness $T_{eff} = 24$, submitted to a hyperfine magnetic field B = 33 T, collinear to $\vec{h}^{\sigma}$ from figure 1.1.

Use of TDSRS as a Hyperfine Technique

In a standard TDSRS measurement, the synchrotron beam is monochromatized down to a level of meV. This energy bandwidth is still 6 orders of magnitude broader than typical linewidths of nuclear levels. The monochromatized radiation interacts with the sample containing Mössbauer-active nuclei. The response of the sample is studied by detecting the scattered radiation as a function of time. This can be done in forward or in Bragg geometry. Many experiments have proved that a precise determination of hyperfine interaction parameters is possible by means of TDSRS. Table 1.2 enumerates the Mössbauer isotopes that have been studied with synchrotron radiation.

Table 1.2: Overview of Mössbauer isotopes measured by means of synchrotron radiation. (State at the beginning of year 2000.)

Isotope	First synchrotron measurement	References
^{57}Fe	1985	[6]
^{169}Tm	1991	[18]
^{119}Sn	1993	[19]
^{83}Kr	1995	[20, 21]
^{181}Ta	1995	[22]
^{151}Eu	1996	[23, 24]
^{161}Dy	1996	[24]
^{40}K	2000	[25]

The advantages of TDSRS compared to conventional Mössbauer spectroscopy are numerous:

1. The high flux density, combined with high directionality of the synchrotron beam enlarges the range of possible measurements. High-pressure experiments with diamond anvil cells [26, 27] and very low temperature experiments are just two examples that benefit from the small beamsize at the sample position.

2. The selected energy band can be tuned to the nuclear resonance one wants to study. Conventional Mössbauer spectroscopy is limited by the availability of a good Mössbauer source for the element in question. For some isotopes, like ^{73}Ge or ^{40}K, there exists no γ-source. (In case of ^{73}Ge this is due to the extremely high internal conversion coefficient.) Nuclear resonance experiments with synchrotron radiation do not depend on this requirement. Most transition energies lie within the tunability range of the undulator.

3. TDSRS can take advantage of the polarization of the incident beam and investigate polarization dependent phenomena.

4. The most obvious advantage of TDSRS is the possibility to study time dependent phenomena.

In spite of all these advantages, TDSRS has one important shortcoming which is precisely connected to the time dependency of the measurement. If one wants to follow the time response of a nuclear system, one should record the nuclear decay during one or two lifetimes of the excited state. This implies that the synchrotron bunches should be spaced by the same amount of time. In case of the 14.413 keV transition in ^{57}Fe, the lifetime is 141 ns and intervals of 100-200 ns are required. Given the fact that third generation synchrotron storage rings have the capacity to give pulses every 2.8 ns, this special time mode for nuclear resonance scattering experiments means a very partial filling of the storage ring and a much lower intensity, which is disadvantageous to users who are measuring simultaneously at other beamlines.
Moreover, the TDSRS method is limited to the study of nuclear levels with relatively short lifetimes. Isomeric states with lifetimes in the order of a few μs (e.g. ^{181}Ta: $\tau = 8.7$ μs) cannot be studied properly due to the finite circumference of the storage ring (period < 4 μs).

To overcome this problem, a new time-integrated method for nuclear resonance scattering of synchrotron radiation is developed [28] which provides the same information on the hyperfine interactions but eases the restrictions related to the nuclear lifetime.

1.3 Time-Integrated Synchrotron-Radiation Spectroscopy (TISRS)

The aim is to avoid the problems connected to TDSRS by performing the measurements in energy domain. Because the incident synchrotron radiation has a broadband spectrum, simply measuring as a function of energy of the incoming radiation is excluded. The idea of TISRS is to do time-integrated experiments by introducing a second, single-line sample which is Doppler modulated. Crossings between transition frequencies in the investigated sample and the variable reference frequency will appear as resonances in the forward-scattered intensity, recorded versus the velocity of the reference sample. This way, a spectrum in energy domain is obtained, similar to a conventional Mössbauer spectrum. Figure 1.3 shows an example of a TISRS spectrum. From the positions, the widths and the amplitudes of the resonances, hyperfine and solid-state information can be derived.

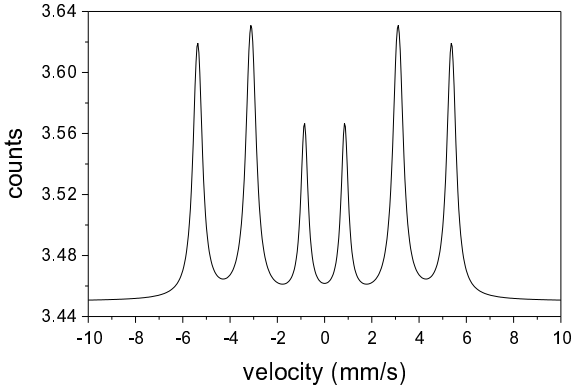

Figure 1.3: Simulation of the TISRS spectrum from a ^{57}Fe absorber with effective thickness $T_{eff} = 20$ and a stainless-steel reference absorber with effective thickness $T_{eff} = 4$. The ^{57}Fe absorber is submitted to a hyperfine magnetic field B = 33 T, oriented perpendicular to the beam direction and under an angle of 45° with respect to the polarization direction of the incident radiation.

Because the measurements are now performed in energy domain, the method does not inherently require a special timing mode and the problem connected to long-lived isomers is solved. Furthermore, the energy spectra are much easier to interpret than the analogous TDSRS spectra.
We think that this new hyperfine technique is an important contribution to the field of nuclear resonance scattering as a complementary method to TDSRS and Mössbauer spectroscopy. We will come back to this later.

1.4 Guide through Following Chapters

In the next chapter, third generation synchrotrons will be discussed. Since the two experiments of this thesis work have been carried out at the Advanced Photon Source in Chicago (U.S.A.), this machine will be taken as an example. The nuclear resonance beamline at the Advanced Photon Source storage ring is sketched and some important beamline components are explained.

The following chapter contains an extensive theoretical description of nuclear resonant scattering by means of time-integrated synchrotron-radiation spectroscopy. The formulae in chapter 3 are given in matrix formalism. The matrix representation allows to modify the formulae in an easy way in case additional components are included in the setup. This is illustrated for the crossed polarizer/analyzer in chapter 5, for a nuclear monochromator in chapter 6, and for an interferometer also in chapter 6. Apart from the theoretical treatment, several simulations of TISRS spectra are given.

Experimental results with the time-integrated nuclear resonant scattering technique are presented in the two subsequent chapters. In the first experiment, reported in chapter 4, it was necessary to put a time gate each time a synchrotron pulse arrived. Otherwise, the electronics would have got overloaded by the high prompt count rate (typically 10^7 counts per second in a 5 meV bandwidth). As a result, the measurement was not completely time-integrated, but rather time-sliced. The consequences of time slicing for TISRS are discussed at length in section 4.2 and a comparison with conventional Mössbauer spectroscopy is given.
In chapter 5, time slicing is reduced to a minimum by adding a crossed polarizer and analyzer to the setup. This experiment yields the expected simple spectra that clearly show the advantages of the time-integrated method. A qualitative comparison with time differential measurements is presented and the use of a polarizer and analyzer in TISRS is discussed.

Finally, several possible improvements of time-integrated nuclear resonant scattering of synchrotron radiation are given in chapter 6. The aim is to enlarge the range of application and to lift the restrictions connected with the polarizer/analyzer setup. Therefore, other solutions for reducing the prompt intensity in the detector need to be found. As a first possibility, the use of a nuclear monochromator is considered. A thorough investigation shows that existing nuclear monochromators are not suited for application in TISRS because of their slow time response. Other solutions, like the development of an ultra fast shutter or an array of ultra thin detectors are mentioned. The only useful extension of TISRS currently available is the inclusion of an X-ray interferometer. This will be explained in section 6.4 and some preliminary simulations will be presented. The implementation of the interferometer in TISRS will be the subject of future research.

Chapter 2

Third Generation Synchrotrons

Since the early nineties, a new generation of synchrotrons has been developed, in which the radiation is generated by undulators. These devices are capable of delivering very intense radiation over a large energy range. The intensity at third generation synchrotrons far exceeds that of their earlier sisters by several orders of magnitude. The enhanced intensity has strongly stimulated nuclear resonance experiments that suffered before from very low resonant count rates. At the moment, several third generation synchrotrons are in use: ESRF in France, APS in the U.S.A. and SPring-8 in Japan. Other synchrotrons, like e.g. HASYLAB in Germany, have been upgraded.

In this chapter a detailed description of third generation synchrotrons is given. The Advanced Photon Source has been taken as an example to explain the acceleration process and the generation of synchrotron radiation. The difference between bending magnet and insertion device radiation is pointed out.
In section 2.2, the nuclear resonance beamline at APS is sketched and a short explanation of the different beamline components is provided. Most of these components are used in the experimental setups that are described in the next chapters.

2.1 The Advanced Photon Source

The Advanced Photon Source (APS) at Argonne National Laboratory, U.S.A., is a third generation synchrotron, operating since 1996. A schematic view of the APS storage ring is shown in figure 2.1.

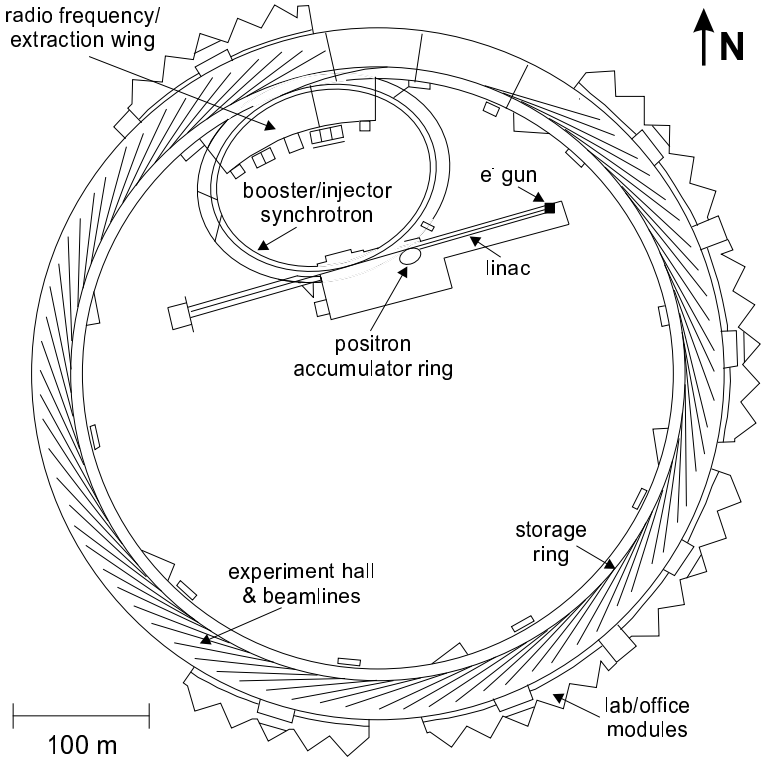

Figure 2.1: Architect's plan view showing the APS accelerating subsystems and experiment-related structures.

The beam acceleration and storage process begins at the electron gun, a cathode-ray tube, which emits electrons at 100 keV. Thirty-ns-long pulses of electrons are raised to an energy of 200 MeV by a first-stage linear accelerator, or linac. Next, the electron beam strikes a 7-mm-thick, water-cooled tungsten disk - the positron conversion target. This interaction creates photons, which produce electron-positron pairs. The APS can operate using either electrons or positrons. In normal operation mode, the second-stage linac is phased to optimize electrons, which are accelerated to 450 MeV.

The positron accumulator ring collects electrons or positrons from the 60 Hz linac during each cycle of the 2 Hz synchrotron. Ten to twelve pulses of electrons are collected in 0.55 sec and injected as one group into the booster synchrotron.

A 386 m long, booster synchrotron raises particle energies at a rate of 32 keV per turn. The accelerating force is supplied by electrical fields within radio-frequency (rf) cavities operating at 352 MHz, the same frequency used by the storage ring rf cavities. During acceleration, the electron bunches will be packed closer together thanks to the principle of phase stability resulting, at the end of the acceleration cycle, in very short pulses ($\pm$ 100 ps). In 0.25 sec, particles orbit the booster 2×10^5 times as their energy climbs to 7 GeV.

Then, the electron beam is injected into the 1.104 km circumference storage ring (SR), located inside the experimental hall (see figure 2.1). The beam is steered and focused by 1097 powerful electromagnets as it travels within a closed system of vacuum chambers running through the magnet centers. Design vacuum inside these chambers is 10^{-9} Torr with beam present. The beam decelerates at a rate of 6 MeV per turn as it emits synchrotron radiation. This energy loss is compensated by the rf cavities in the storage ring. Every 10-20 hours, the SR is refilled.

Storage Ring

A storage ring is configured as a set of curves connected with straight sections. When a charged particle is accelerated so that either its speed or trajectory changes, radiation will be emitted. The particles (electrons or positrons) that orbit the APS storage ring are accelerated when their trajectory is altered by the bending magnets that make the beam travel in a circle. The X-rays emitted at each of these bends go off in a direction tangential to the arc of the particle beam. All around the storage ring 80 bending magnets are present. Thirty-five of them are accompanied by beam ports to extract the synchrotron radiation.

Besides the bending magnets another type of devices is used to generate radiation: the insertion devices. These are linear arrays of north-south permanent magnets with alternating polarity. They are inserted into the straight sections, one array above the beam path, the other below (figure 2.2). When the charged particles pass through the alternating fields, they either wiggle or undulate, depending on the configuration of the insertion device. This action greatly enhances the synchrotron radiation. In wigglers, a high magnetic field and a relatively greater distance between the individual magnets produces very intense radiation over a wide and continuous range of energies. The magnets in undulators have a lower field

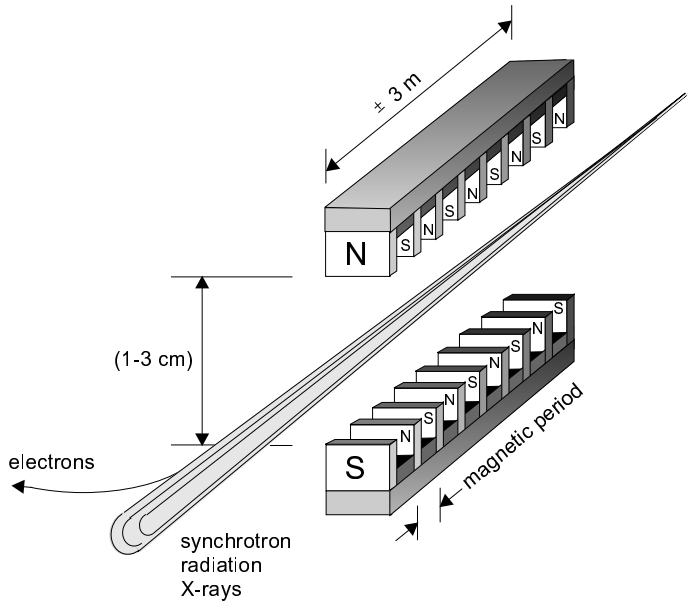

Figure 2.2: Insertion device.

than those in wigglers, and they are spaced closer together. The lower magnetic field in undulators narrows the cone of radiation, allowing all of the radiation from each pole to interfere constructively. This interference creates peak intensities at certain energies.

Storage rings optimized for insertion devices are "third generation" synchrotron light sources. Some, like the Advanced Light Source (ALS) in California, and the SuperACO in France, provide radiation in the ultraviolet/soft X-ray part of the spectrum. The 7 GeV APS and its sister facilities, the 6 GeV European Synchrotron Radiation Facility (ESRF) in France and the 8 GeV Super Photon Ring (SPring-8) in Japan, can produce a range of X-rays up to those of the hard (highly penetrating) variety because of higher machine energies.

Third generation storage rings are characterized by very high flux and brilliance of the X-ray beam. Flux is the number of photons per second passing through a defined area, and is the appropriate measure for experiments that use the entire, unfocused X-ray beam. Brilliance is a measure of the intensity and directionality of an X-ray beam. It is defined as the number of photons per second in a narrow energy band-width and in a unit of solid angle in the horizontal and vertical directions. It determines the smallest spot onto which an X-ray beam can be focused.

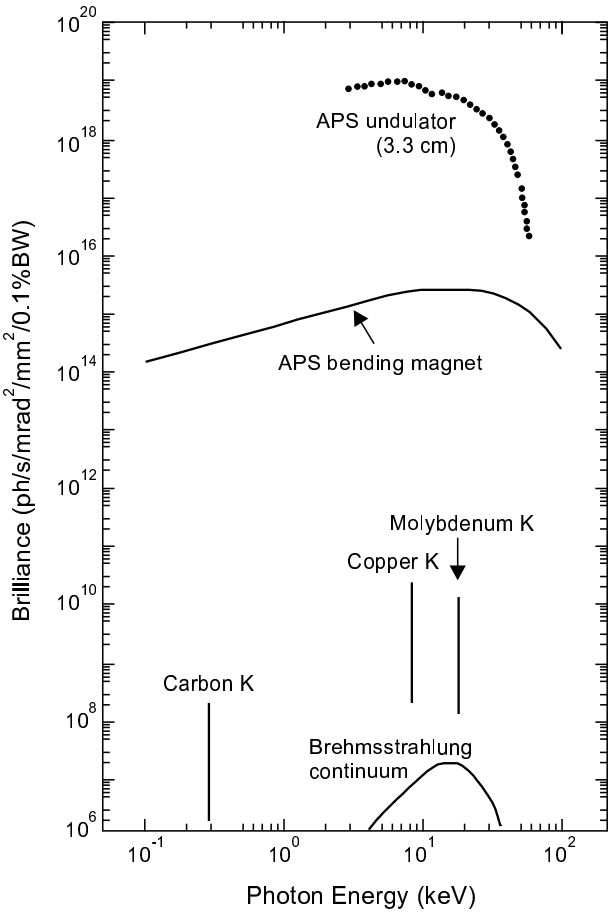

Figure 2.3: APS spectral brilliance compared to a variety of conventional ultraviolet and X-ray tube sources.

Figure 2.3 shows APS spectral brilliance for bending magnets and undulators and compares them to conventional ultraviolet and X-ray tube sources. A standard APS undulator is capable of delivering high-brilliance beams in the hard X-ray region from 2.5 keV to ±60 keV. Bending magnet radiation sources at the APS also have unique capabilities because of their high brilliance, particularly above 20 keV.

Synchrotron light produced by bending magnets and insertion devices goes to the different beamlines inside the experimental hall. The insertion device and bending magnet beamlines emerge from the synchrotron enclosure as pairs, each pair constituting a sector. The APS storage ring is divided in 40 sectors. Five of the sectors are taken up with beam injection and rf equip-

ment. The remaining 35 are equipped to provide synchrotron radiation. A typical APS storage ring sector is shown in figure 2.4.

Radiation is transported from the synchrotron to the research beamlines through beamline front ends, which are positioned immediately outside the technical components of the synchrotron, but still inside the concrete synchrotron shielding tunnel. The front ends contain safety shutters, photon beam stops, and other components to coarsely define the emerging X-ray beam and, if required, to stop the X-ray beam and provide adequate radiation protection to areas outside the shielding tunnel. Normal incidence heat fluxes in the insertion device front ends are on the order of 450 W/mm^2 or higher, and total heat loads approach 10-15 kW.

The research beamlines comprise X-ray optical elements that tailor the beam to the scientist's needs. These elements are generally contained in the first optics enclosure adjoining the outside of the synchrotron enclosure and include monochromators, filters, and/or mirrors. These optics select out about one part per million from the energies (or wavelengths) that are carried by the insertion device beam, and pass that energy down the beamline to the research station.

The research stations contain experimental instruments, the sample under investigation, detectors and any additional optics needed to analyze and characterize the scattering, absorption or imaging process. Some of the photon beams are split, so that each beamline can have additional branch lines and numerous experimental stations.

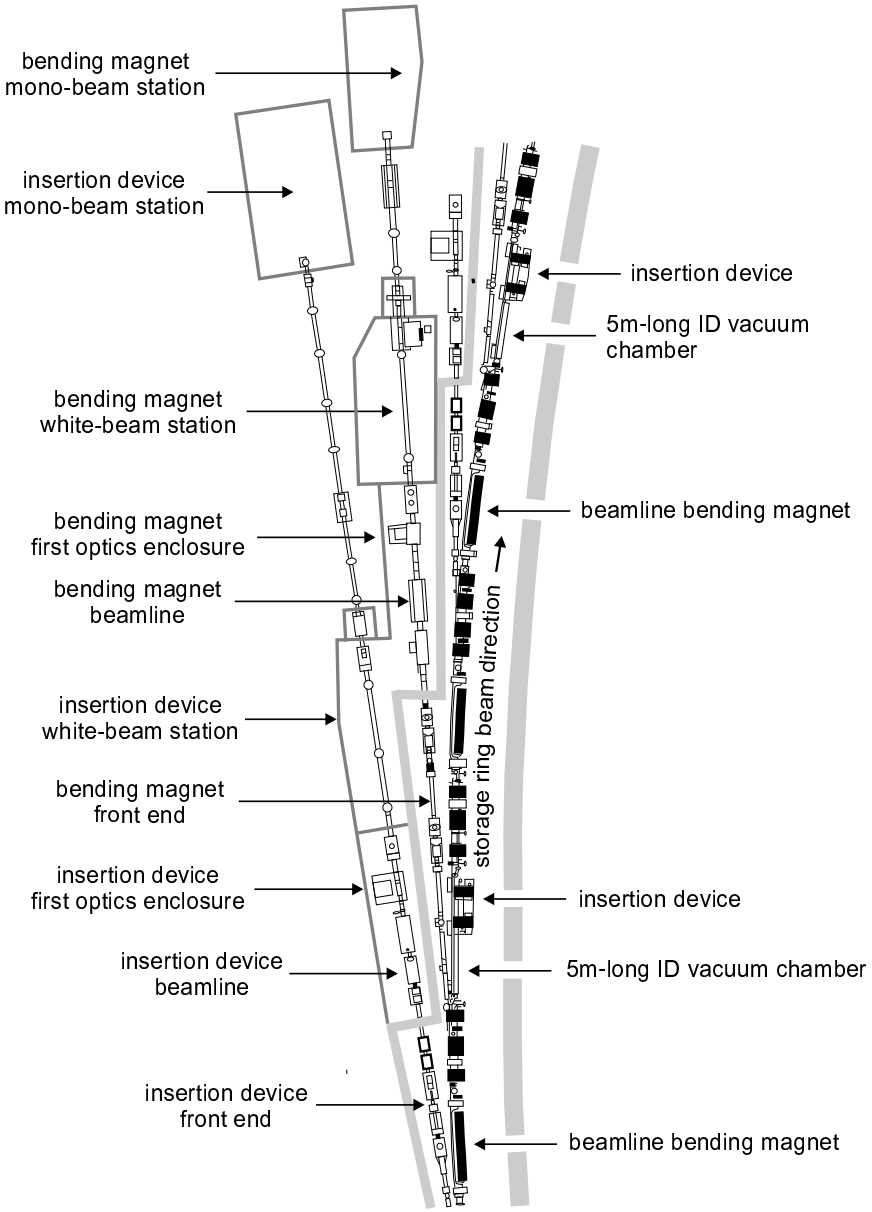

Figure 2.4: Diagram of a typical sector at APS, taken from Ref. [29]

2.2 Nuclear Resonance Beamline

The experiments reported in this work have been carried out at the 3ID undulator beamline at APS, dedicated to nuclear resonant scattering experiments. Details on this beamline can be found in Ref. [30].

Synchrotron radiation is generated by a 2.5 m-long undulator [31, 32] with a magnetic period of 2.7 cm. The undulator is tunable to deliver X-ray energies between 6 keV and 16 keV in the first harmonic. When going to higher-order harmonics, energies till 30 keV and higher can be reached. Table 2.1 shows some characteristics of the Mössbauer isotopes within the tunability range of the undulator.

When tuned to the 14.413 keV nuclear resonance of ^{57}Fe, the flux density right after the undulator is 2.4×10^{13} photons/(s eV) for 100 mA electrons stored in the ring.

Table 2.1: Properties of several Mössbauer-active isotopes within the tunability range of an APS undulator.

Isotope	E_0 (keV)	τ (ns)	Γ_0 (mm/s)	α	abund. (%)
^{181}Ta	6.214	8730.0	0.003	70.5	99.99
^{169}Tm	8.410	5.8	4.048	268	100.00
^{83}Kr	9.404	212.1	0.099	19.6	11.55
^{133}Ba	12.290	11.7	1.373	110	0.00
^{73}Ge	13.263	4260.3	0.003	1095	7.76
^{57}Fe	14.413	141.1	0.097	8.19	2.14
^{151}Eu	21.542	14.0	0.668	28.6	47.82
^{149}Sm	22.494	10.3	0.852	50	13.83
^{119}Sn	23.871	25.8	0.321	5.12	8.58
^{161}Dy	25.655	40.7	0.189	2.9	18.88
^{129}I	27.770	24.2	0.294	5.1	0.00
^{40}K	29.830	6.1	1.095	0.29	0.01

E_0: transition energy, τ: lifetime of nuclear level, Γ_0: nuclear level width, α: internal conversion coefficient, abund.: natural abundance of the Mössbauer isotope

The X-ray beam generated by the undulator enters the first hutch. Inside, the beam is collimated by means of slits. Additionally, the bandwidth of the incoming radiation is reduced by a high-heat-load monochromator, capable of handling large power loads. The energy bandpass after the high-heat-load monochromator in absence of other optical components is reduced to

3.5 eV around the 14.413 keV resonance energy. The total flux at this point is 3×10^{12} photons/s. Other components such as a compound refractive lens and a dynamically bent crystal can also be placed in this first hutch.

Next, the pre-monochromatized photon beam enters the experimental station. The unfocused X-ray beam at this point is about 1.8 mm high and 3.5 mm wide. For nuclear resonance experiments the X-ray beam needs to be further monochromatized. This can be achieved by a high-energy-resolution monochromator or by polarizer and analyzer crystals. Finally, the radiation interacts with the sample under investigation and the scattered radiation is registered by a fast detector.

Figure 2.5 shows a typical beamline setup. In the next section, the different components will be explained.

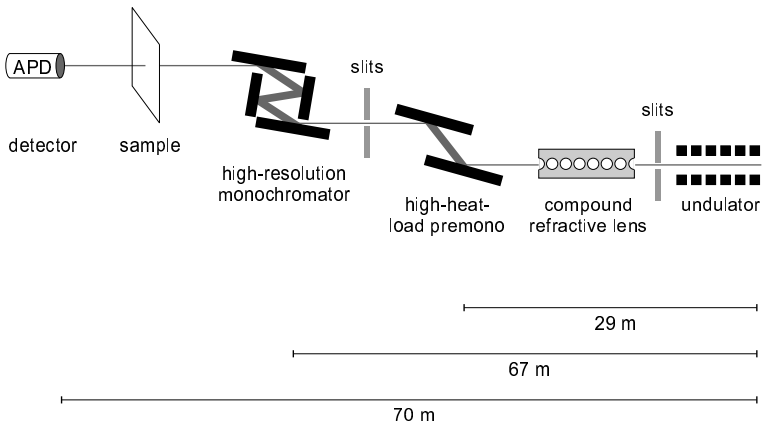

Figure 2.5: Example of a beamline setup for nuclear resonant scattering experiments. Note that the direction of the synchrotron beam is from right to left. Some characteristic distances from the source point are indicated.

2.2.1 Beamline Components

High-Heat-Load Monochromator

The principal optical component in the beamline is the high-heat-load monochromator. It consists of two Si(1 1 1) crystals, placed at 29 m from the source point. The crystals are cut asymmetrically by 4° so as to increase the angular acceptance of the Bragg reflection.

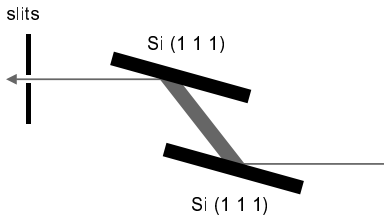

Figure 2.6: High-heat-load monochromator.

For the ^{57}Fe resonance Si(1 1 1) Bragg reflections are used, which select an energy bandpass of 3.5 eV around 14.413 keV. The second crystal improves the energy selection of the first crystal and provides an exit beam which is collinear to the primary beam. This is important from a practical point of view, since all subsequent equipment can be aligned in the horizontal plane.
The vertical distance between both monochromator crystals can be varied in order to reduce the background caused by the primary beam. This is achieved by means of slits. See figure 2.6.

The beam incident on the first crystal has an enormous power load (up to 4 kW with a power density of 140 W/mrad^2). Therefore, it is necessary to cool the first Si crystal. This can be done with water, liquid Gallium or liquid Nitrogen. Moreover, due to changing heat loads, the temperature of the crystals should be stabilized.

Compound Refractive Lens

In order to obtain a focus in vertical direction before the high-heat-load monochromator, one can use a compound refractive lens [33]. This is a block of low Z-material with several cylindrically drilled holes. It focuses the X-ray beam to a beamspot of ≤ 1 μm and increases the intensity in the focal spot.

Figure 2.7 shows a schematic diagram of a compound refractive lens consisting of a linear array of many simple lenses manufactured in low Z-material,

such as, e.g., Be, B, C, Al. One chooses low-atomic weight materials in order to minimize absorption. On the other hand, refraction effects for X-rays in matter are usually extremely small. Therefore, several lenses (holes) are put one after the other along the optical axis. This way, refraction is increased and the focal length F is decreased, since it scales with the inverse of the number of holes N:

$$F = \frac{R}{2N\delta}$$

where R is the radius of the lens and δ is the refractive index decrement. Typically δ is in the order of $10^{-5} - 10^{-7}$ for X-rays. As an example, for an Aluminum compound refractive lens with 30 holes, the focal length is reduced from 54 m for an individual lens to 1.8 m. The number of holes depends on their radius and on the X-ray energy. Typically, hole radii are in the range of 250-600 μm. These dimensions nicely match the beam size of third generation synchrotron-radiation sources ($\pm$ 100 μm).

The main advantage of focusing the undulator X-ray beam by a compound refractive lens is the intensity gain in the focal spot as compared to the intensity one would obtain in a similar spot using a collimated pinhole or slit. For 14 keV X-rays, this gain is easily a factor of 3. Compound refractive lenses are very efficient for focusing X-rays in the energy range of 5-40 keV.

For nuclear resonant scattering, a compound refractive lens can be put in front of the high-heat-load monochromator, in order to focus the X-ray beam in vertical direction. This configuration will increase the intensity output of the monochromator since a larger portion of the incoming beam lies in the acceptance range of the high-heat-load monochromator. The compound refractive lens as shown in figure 2.7 only focuses in one direction. Focusing in horizontal direction is not really needed at this point since the high-heat-load monochromator has a large horizontal acceptance.

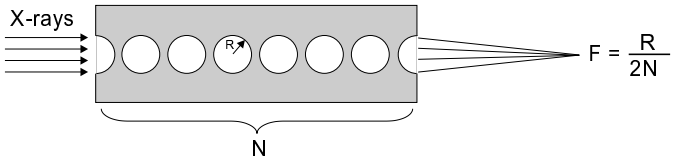

Figure 2.7: Schematic diagram showing the principles of X-ray focusing by a compound refractive lens. It consists of a number (N) of cylindrical holes placed close together in a row along the optical axis and focuses the X-rays at a distance that is N times shorter as compared to a single lens.

High-Energy-Resolution Monochromator

A second electronic monochromator can be used to further reduce the bandwidth of radiation coming from the high-heat-load crystals. For this purpose, a nested monochromator, consisting of symmetrical and asymmetrical channel-cut crystals, is used [34]. By combining high-order reflections with an asymmetric channel-cut, one can achieve high energy resolution and large angular acceptance.

The energy resolution for Bragg diffraction from perfect single crystals can be approximated by

$$\frac{\Delta E}{E} \approx \Delta\theta \; cot(\theta_B)$$

θ_B is the Bragg angle and $\Delta\theta$ the incident divergence. Choosing high-order reflections (i.e. large Bragg angles), the energy resolution improves. But, in a symmetrically cut single crystal, the gain in resolution is accompanied by a loss of angular acceptance. This ambiguity can be solved by cutting the crystal asymmetrically, at an angle α with respect to the diffracting planes. Then, the angular acceptance will be increased by a factor

$$\frac{\sin(\theta_B + \alpha)}{\sin(\theta_B - \alpha)}$$

High-order reflections from asymmetrically cut single crystals yield both a high energy resolution and a high angular acceptance.

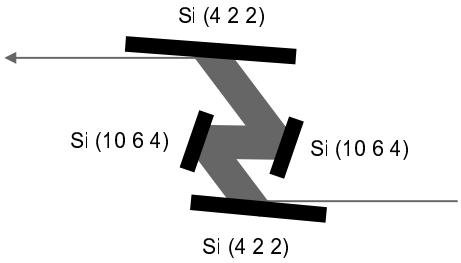

Figure 2.8: High-energy-resolution monochromator for 14.413 keV radiation [35].

The high-resolution monochromator at the 3ID-beamline, optimized for selecting 14.413 keV radiation, is shown in figure 2.8. The outer crystal pair is a Si(4 2 2) channel-cut crystal with an asymmetry angle of -20°. The inner pair is a symmetrically cut Si(10 6 4) crystal. The monochromator has an energy bandpass of 5.5 meV at the ^{57}Fe resonance, and accepts $\pm$ 22 μrad of a diverging beam. The throughput of the monochromator at 14.413 keV is better than 60%.

Crossed Polarizer and Analyzer

Instead of a high-resolution monochromator, a crossed polarizer and analyzer can be used to suppress the nonresonant radiation [36]. The polarizer is placed directly after the high-heat-load monochromator. Then follows the investigated sample and the analyzer. Only resonant radiation that has interacted with the sample can pass the analyzer.

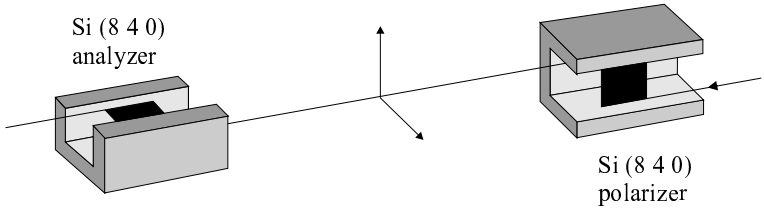

Figure 2.9: Illustration of the polarizer/analyzer setup.

The performance of a polarizer for X-rays is based on the fact that the angular acceptance of a perfect crystal depends on the polarization of the incident beam. Following the convention that σ and π polarization are defined by, respectively, electromagnetic radiation having the electric field vector perpendicular or parallel to the scattering plane, the following rule holds: for σ-polarized radiation, the additional factor to the angular acceptance is unity, while for π-polarized radiation it is given by $\cos(2\theta_B)$. Thus, for Bragg angles close to 45°, the angular acceptance for the π component will be close to zero.

The crossed polarizer and analyzer at the 3ID undulator beamline at APS, designed for the 14.413 keV resonance, is described in Ref. [37]. It consists of two Si (8 4 0) channel-cut crystals with an asymmetry angle of -43°. The Bragg angle is $\theta_B = 45.1°$. The first crystal, the polarizer, is used to linearly polarize the synchrotron radiation generated by an undulator source at the 14.413 keV nuclear resonance of ^{57}Fe. This crystal only transmits σ-polarized radiation. It reduces the energy bandwidth of the synchrotron radiation to 0.32 eV around resonance.
The second crystal, the analyzer, is turned over 90° so that it only transmits π-polarized light. If in between both crystals a resonant sample is present, then the nuclear scattered radiation will undergo $\sigma \rightarrow \pi$ polarization conversion. The nonresonant radiation, however, will remain σ-polarized and is filtered out by the analyzer. A suppression factor of $6 \cdot 10^{-7}$ can be obtained. After the analyzer, the energy bandwidth is of the order of neV.

As will be shown in chapter 3, nuclear resonant forward scattering of synchrotron radiation can only introduce polarization changes if the resonant sample is submitted to a hyperfine interaction. Moreover, the fields acting on the nuclei should have well defined orientations. As a consequence, the polarizer/analyzer setup cannot be applied for single-line samples or samples submitted to randomly oriented hyperfine fields.

Avalanche Photodiode Detector

Time differential experiments using nuclear resonant scattering of synchrotron radiation require a γ-ray detector with good time resolution and high signal-to-noise ratio. The detector should cover the energy range from 6-20 keV. Avalanche Photodiode Detectors (APD's) with subnanosecond time resolution meet these requirements.

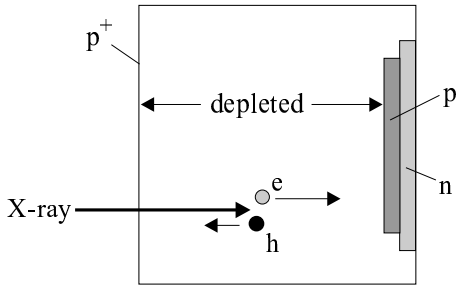

Figure 2.10: Structure of a reach through APD [38].

Figure 2.10 shows the structure of a reach through APD. As voltage is applied, the depletion region reaches through to the front contact, and leads to a region of extremely high field near the junction where avalanche gain takes place. X-rays are photo-electrically absorbed in the bulk of the device, creating an electron-hole (e-h) pair per 3.6 eV of incident energy. The electrons drift to the gain region where they are amplified. The active thickness, i.e. the part of the depletion region where X-ray absorption will lead to amplification, determines the efficiency of the detector at energies above a few keV. More information on composition and operation of APD's can be found in Ref. [39].

For an active thickness of more than 90 μm of silicon, the efficiency varies from $\approx 70\%$ at 8 keV to $\approx 15\%$ at 16 keV [40]. The efficiency decreases with increasing photon energy. A single APD is reasonably efficient at normal incidence up to X-ray energies of 20 keV. The efficiency can be increased by tilting the detector (e.g. under 60°), thus increasing the X-ray path length

in the active region of silicon [39]. When several APD's are stacked one after the other, higher energies, up to 30 keV, can be detected with good efficiency [38].

The most important characteristic of an APD is its extremely good time resolution. Depending on the thickness of the depletion layer, a resolution down to 100 ps (FWHM) can be reached [41] (which is far better than scintillation detectors can achieve [42]). The dead time of the detector is also short ($\approx$ 10 ns at 3.8 10^7 Hz) [38, 43]. The time response of an APD is essentially a Gaussian peak with a short tail [44]. The full width at 10^{-5} of the peak maximum is only 1.4 ns [41].

Moreover, APD's have a large dynamic range. The noise rate is 10^{-2} Hz and the upper limit for linear response is 10^7 Hz. This yields a dynamic range of nine orders of magnitude [45].

APD's may be considered as an alternative to, and, for some applications, an improvement over the standard scintillator/photomultiplier (PMT) combination [46]. APD's have comparable efficiency for low-energy X-rays but are much faster and allow higher count rates. The latter is very important at third generation synchrotron-radiation sources with count rates of $10^9 - 10^{10}$ Hz. In addition, the energy resolution of APD's is similar to a NaI/PMT combination but the timing properties are much better.

Typical applications where APD's are used, are nuclear resonant scattering studies requiring a good timing resolution, or experiments in which a fast recovery from the synchrotron burst is needed, as will be the case for the experiments reported in this work. Moreover, APD's are especially suited for bunch purity measurements of synchrotron X-ray beams [41].

Chapter 3

Time-Integrated Synchrotron-Radiation Spectroscopy

In this chapter, time-integrated synchrotron-radiation spectroscopy (TISRS) using nuclear resonant scattering of synchrotron radiation is explained. The first section gives an intuitive explanation of the method. A more profound, theoretical description follows in section 3.2. The semiclassical optical model for radiation [13] is used to derive an expression for the time-integrated forward-scattered intensity. The two most important formulae are Eq. (3.4) for the elastic nuclear forward scattering amplitude and Eq. (3.10) for the amplitudes of transmitted radiation in TISRS. Two special cases in which the hyperfine fields either vanish, or are randomly distributed are discussed.

Finally, in the last section, simulations of TISRS spectra are presented for the magnetic dipole transition between the ground state and the first excited state in ^{57}Fe. The case of a single-line sample is worked out explicitly, and two simulations for different sample thicknesses are presented. For samples submitted to a magnetic hyperfine field, it is shown that the TISRS spectra are sensitive to the orientation of the magnetic field with respect to the photon beam and also with respect to the linear polarization direction of the synchrotron radiation. This interesting property distinguishes TISRS from conventional Mössbauer spectroscopy.

3.1 Description of the Method

The aim of time-integrated synchrotron-radiation spectroscopy (TISRS) is to perform measurements in energy domain. Since the incoming synchrotron radiation has a broadband spectrum ($\Delta E \gg \Gamma$), simply measuring as a function of energy of the incoming radiation is excluded. Hence, in addition to the investigated sample, a single-line reference sample is introduced, which is mounted on a Mössbauer drive. Due to the velocity, the nuclear transition frequency will be Doppler modulated, according to $\omega_r = \omega_0 (1 + v/c)$, where v and c have the usual meaning of velocity and speed of light, ω_0 is the nuclear transition frequency in absence of any Doppler modulation, and ω_r is the modulated transition frequency in the reference. In the investigated sample, there can be several nuclear transitions, depending on the hyperfine interaction. This sample is kept stationary and, consequently, all frequencies will be constant. (See figure 3.1.)

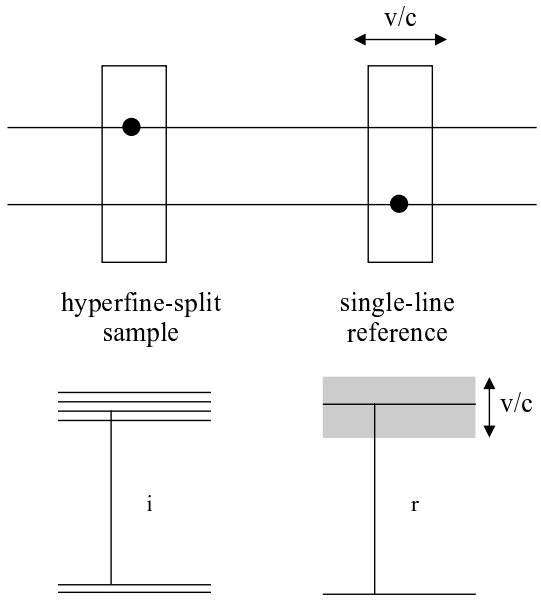

Figure 3.1: Schematic picture of the TISRS method.

Due to space coherence, synchrotron radiation can excite all nuclei in the sample and the reference coherently. The coherence length is typically several meters. Moreover, the incoming synchrotron photon has a broadband spectrum and will excite all nuclear transition frequencies within its spectral band. This is known as energy coherence. The coherent excitation of different energy levels gives rise to interferences in the scattered intensity. An example of spatial coherence is shown in the upper part of figure 3.1:

A single photon can be resonantly scattered on the sample, or on the reference, yielding an interference between both scattering paths. When the scattered radiation is measured as a function of time, the interferences will show up as quantum beats with beat frequencies corresponding to the energy differences of all allowed transitions from all different nuclear sites [16]. However, if the time-averaged intensity is measured, the quantum beats will level out, except when the beat period becomes comparable to or larger than the nuclear lifetime of the excited state. This happens when the reference frequency ω_r matches one of the transition frequencies in the sample. For thin samples, the forward-scattered intensity can be written as [47]:

$$I_{fs} = N_s^2 + N_r^2 + \sum_i \frac{2\, N_s\, N_r}{(\omega_i - \omega_r)^2\, \tau^2 + 1} \tag{3.1}$$

N_s and N_r are proportional to the number of resonant nuclei in the sample and reference respectively, and τ is the nuclear lifetime of the excited state. The first two terms, $N_s^2 + N_r^2$, are constant. The summation in the third term runs over all nuclear transition frequencies ω_i in the investigated sample. Measuring the nuclear resonant forward-scattered radiation as a function of the reference's velocity yields a spectrum in energy domain. Whenever ω_r is equal to one of the ω_i, the last term in Eq. (3.1) will give an extra contribution, seen as a resonance. This is shown schematically in figure 3.2.

The TISRS spectrum is very similar to a conventional Mössbauer spectrum. From the positions, the widths, and the amplitudes of the resonances, hyperfine and solid-state information can be obtained, similar as in Mössbauer spectroscopy. For thick samples Eq. (3.1) becomes more complicated, but the basic features remain [47, 48]. A general expression for the time-integrated forward-scattered intensity, that is also valid for thick samples, will be derived in the next sections.

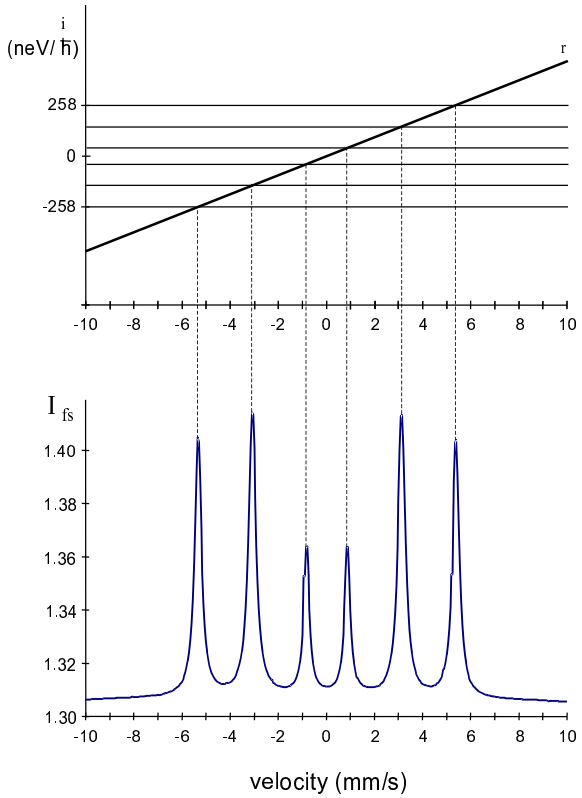

Figure 3.2: Illustration of TISRS for a magnetically split ^{57}Fe sample and a single-line reference. The effective thicknesses are 5 and 1, respectively. Top: Transition frequencies in the sample (horizontal lines) and reference (inclined line) normalized to 14.413 keV. Bottom: The corresponding TISRS simulated spectrum.

3.2 Theory of TISRS

3.2.1 Resonant Scattering on a Bound Nucleus

If a γ-ray is scattered by an individual nucleus bound in a lattice, the amplitudes of the incoming and scattered waves, $\vec{A}_{in}$ and $\vec{A}_{sc}$ respectively, are connected via

$$\vec{A}_{sc} = f\vec{A}_{in}$$

The factor f is the nuclear scattering amplitude. It is a complex function of the energy of incoming radiation.

A general expression for the nuclear scattering amplitude taking into account hyperfine splitting of the nuclear levels is derived in Refs. [49, 50]. Consider the case where the fields acting on the nucleus have a common symmetry axis. A generalization for asymmetric electric field gradients or electric field gradients that are noncollinear to the magnetic field can be found in Ref. [49]. Let $\hat{z}$ be the symmetry axis of the nuclear system.

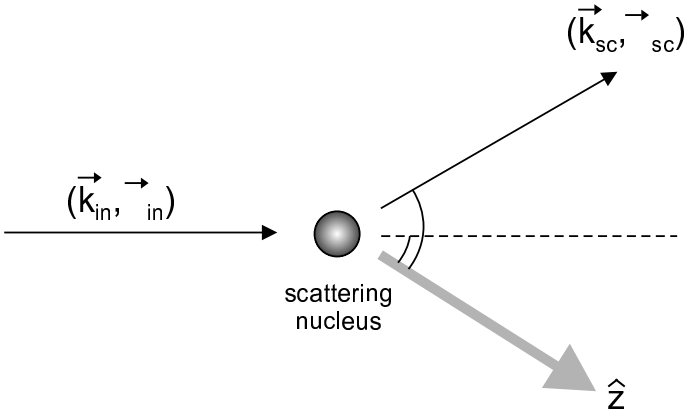

Figure 3.3: Scattering of a photon by a bound nucleus. $\hat{z}$ is the symmetry axis of the hyperfine fields acting on the nucleus.

If an incident photon with wave vector $\vec{k}_{in}$ and circular polarization $\vec{\sigma}_{in}$ is scattered into a photon with wave vector $\vec{k}_{sc}$ and circular polarization $\vec{\sigma}_{sc}$ while the nucleus makes a multipole transition from an initial state $\mid j_g, m_g >$ over an excited state $\mid j_e, m_e >$ to a final state $\mid j'_g, m'_g >$, then the nuclear scattering amplitude is given by

$$f\,(\vec{k}_{in},\vec{\sigma}_{in}\rightarrow\vec{k}_{sc},\vec{\sigma}_{sc}) \;=\; \frac{1}{4k_{sc}}\,f_{LM}$$
$$\times\sum_{L,\Lambda,\Delta}\;\sum_{L',\Lambda',\Delta'}\sigma_{in}^{(\Lambda+1)}\sigma_{sc}^{(\Lambda'+1)}\sqrt{(2L+1)(2L'+1)}\,\sqrt{\gamma_R(L,\Lambda)\gamma_R(L',\Lambda')}$$
$$\times\,C(j_gLj_e;m_g\Delta m_e)\,C(j_g'L'j_e;m_g'\Delta'm_e)\,\mathcal{D}^{(L)*}_{\sigma_{in}\Delta}(\alpha\beta\gamma)\mathcal{D}^{(L')}_{\sigma_{sc}\Delta'}(\alpha'\beta'\gamma')$$
$$\times\,\frac{1}{E_{in}-(E_{m_e}-E_{m_g})+i\Gamma/2} \qquad (3.2)$$

f_{LM} is the Lamb-Mössbauer factor. $\gamma_R(L,\Lambda)$ is the partial linewidth of the nuclear excited state for radiative multipole transition. (L,Λ) with $\Lambda=0,1$ designates the multipole: $(L,0)\equiv M(L)$ is a magnetic 2^L pole, while $(L,1)\equiv E(L)$ is an electric 2^L pole. $\sigma_{in},\sigma_{sc}=+1,-1$ define the right- and left-handed circular polarization state, respectively.

In formula (3.2), the $C(j_gLj_e;m_g\Delta m_e)$-factors are the Clebsch-Gordan coefficients. They are zero unless $\Delta=m_e-m_g$. These factors give the relative strength of a particular transition. The rotation matrices $\mathcal{D}^{(L)}_{\sigma\Delta}(\alpha\beta\gamma)$ describe the angular dependence of the excitation and emission process, taking into account the polarization of the incoming and scattered radiation and the multipolarity of the transition. They also depend on the propagation direction of the photons via the Euler angles $(\alpha\beta\gamma)$, which describe the rotation from the radiation axis system to the principal axis system of the hyperfine fields. The notation of Rose [51] has been adopted.

The last line in Eq. (3.2) gives the energy dependence of the nuclear scattering. E_{in} refers to the energy of the incoming radiation, whereas $E_{m_e}-E_{m_g}$ is the transition energy between the excited and the initial state.

The following of this work will be limited to elastic nuclear scattering in the forward direction ($\vec{k}_{in}=\vec{k}_{sc}$ and $\mid j_g',m_g'>\;=\mid j_g,m_g>$). Furthermore, only transitions with a single, well defined multipole character are considered, so that $L=L'$ and $\Lambda=\Lambda'$. The expression for the elastic nuclear forward scattering amplitude now simplifies to

$$f\,(\vec{k}_{in},\vec{\sigma}_{in}\rightarrow\vec{k}_{in},\vec{\sigma}_{sc}) \;=\; \frac{1}{4k_{in}}\,f_{LM}\,\sigma_{in}^{(\Lambda+1)}\,\sigma_{sc}^{(\Lambda+1)}\,(2L+1)\,\gamma_R$$
$$\times\sum_{\Delta}C^2(j_gLj_e;m_g\Delta m_e)\,\mathcal{D}^{(L)*}_{\sigma_{in}\Delta}(\alpha\beta\gamma)\,\mathcal{D}^{(L)}_{\sigma_{sc}\Delta}(\alpha\beta\gamma)$$
$$\times\,\frac{1}{E_{in}-(E_{m_e}-E_{m_g})+i\Gamma/2} \qquad (3.3)$$

If the incoming γ-ray has a broadband spectrum, as is the case for synchrotron radiation, all hyperfine transitions can be excited at once. This means one has to sum equation (3.3) over all initial and excited spin states. The sum over the ground state levels is a weighed sum, taking into account the probability of finding a nucleus in a particular ground state level. Here, equal probability for all ground state sublevels will be taken (which is a good approximation at room temperature since the energy splittings are much less then $k_B T$).

$$f\,(\vec{k}_{in},\vec{\sigma}_{in} \rightarrow \vec{k}_{sc},\vec{\sigma}_{sc}) \Rightarrow \frac{1}{2j_g+1}\sum_{m_g}\sum_{m_e} f\,(\vec{k}_{in},\vec{\sigma}_{in} \rightarrow \vec{k}_{sc},\vec{\sigma}_{sc})$$

Finally, when the crystal is not exclusively composed of resonant nuclei, Eq. (3.3) should be multiplied by the isotropic enrichment of the sample, χ. Using the definition of the maximal resonant-scattering cross section

$$\sigma_0 = \frac{2\pi}{k_{in}^2}\,\frac{\gamma_R}{\Gamma}\,\frac{2j_e+1}{2j_g+1}$$

one can write the elastic nuclear forward scattering amplitude for synchrotron radiation as

$$\begin{aligned} f\,(\vec{k}_{in},\vec{\sigma}_{in} \rightarrow \vec{k}_{in},\vec{\sigma}_{sc}) \;=\; & \frac{k_{in}}{8\pi}\,\sigma_0\, f_{LM}\,\chi\,\sigma_{in}^{(\Lambda+1)}\,\sigma_{sc}^{(\Lambda+1)}\,\frac{2L+1}{2j_e+1} \\ & \times \sum_{m_g}\sum_{m_e}\sum_{\Delta} C^2(j_g L j_e; m_g \Delta m_e)\,\mathcal{D}^{(L)*}_{\sigma_{in}\Delta}(\alpha\beta\gamma)\,\mathcal{D}^{(L)}_{\sigma_{sc}\Delta}(\alpha\beta\gamma) \\ & \times \frac{\Gamma}{E_{in}-(E_{m_e}-E_{m_g})+i\Gamma/2} \end{aligned} \tag{3.4}$$

Equation (3.4) is the general expression for the elastic nuclear scattering amplitude in forward direction using synchrotron radiation. It is dependent on the photon direction $\hat{k}_{in}$ relative to the symmetry axis $\hat{z}$ of the hyperfine fields via the product of the rotation matrices. For axially symmetric hyperfine fields, the third Euler angle can be taken as zero ($\gamma = 0$). The two other Euler angles are related to the spherical coordinates (θ,φ) of the symmetry axis of the hyperfine fields with respect to the radiation axis system, via: (α,β) = (φ,θ).

The elastic nuclear scattering amplitude is in fact a 2×2 matrix, which can be written in the form:

$$\begin{bmatrix} f^{++}(\omega) & f^{+-}(\omega) \\ f^{-+}(\omega) & f^{--}(\omega) \end{bmatrix}$$

Here, a new notation is introduced:

$$f\,(\vec{k}_{in}, \vec{\sigma}_{in} \rightarrow \vec{k}_{in}, \vec{\sigma}_{sc}) = f^{\sigma_{in}\,\sigma_{sc}}(\omega = c\,k_{in})$$

The non-diagonal terms describe scattering processes that change the polarization state of the photon. Under specific conditions, these terms become zero, as will be shown below.

Unsplit Line

Consider the case where no hyperfine splitting of the nuclear levels is present. Then, there is only one resonance energy, which can be put in front of the summations in Eq. (3.4). Using the orthogonality relations for the Clebsch-Gordan coefficients

$$\sum_{m_e} \sum_{m_g} C^2(j_g L j_e; m_g \Delta m_e) = \frac{2j_e + 1}{2L + 1}$$

and the following relationship for the rotation matrices [51]:

$$\sum_{\Delta} \mathcal{D}^{(L)*}_{\sigma_{in}\,\Delta}(\alpha\beta\gamma)\, \mathcal{D}^{(L)}_{\sigma_{sc}\,\Delta}(\alpha\beta\gamma) = \delta_{\sigma_{in},\sigma_{sc}}$$

a simple form for the nuclear elastic scattering amplitude is obtained:

$$\begin{bmatrix} f^{++}(\omega) & f^{+-}(\omega) \\ f^{-+}(\omega) & f^{--}(\omega) \end{bmatrix} = \frac{k_{in}}{8\pi} \frac{\sigma_0\, f_{LM}\, \chi\, \Gamma}{E_{in} - (E_{j_e} - E_{j_g}) + i\Gamma/2} \begin{bmatrix} 1 & 0 \\ 0 & 1 \end{bmatrix}$$

The unitary matrix indicates that, for a single-line, the scattered photon has the same polarization as the incident one.

Randomly Oriented Hyperfine Fields

Another example where the non-diagonal terms vanish, is when the hyperfine fields are randomly oriented in the sample. Then, one has to average Eq. (3.4) over all Euler angles. From the orthogonality property of rotation matrices on the unit sphere [51]:

$$\frac{1}{8\pi^2}\int_0^{2\pi} d\alpha \int_0^{\pi} d\beta \sin\beta \int_0^{2\pi} d\gamma\, \mathcal{D}^{(L)*}_{\sigma\Delta}(\alpha\beta\gamma)\, \mathcal{D}^{(L')}_{\sigma'\Delta'}(\alpha\beta\gamma) = \frac{1}{2L+1}\,\delta_{\sigma,\sigma'}\,\delta_{\Delta,\Delta'}\,\delta_{L,L'}$$

the following expression for the elastic nuclear scattering amplitude is obtained:

$$\begin{bmatrix} f^{++}(\omega) & f^{+-}(\omega) \\ f^{-+}(\omega) & f^{--}(\omega) \end{bmatrix} = \frac{k_{in}}{8\pi}\frac{1}{2j_e+1}\sum_{m_g}\sum_{m_e}\sum_{\Delta} C^2(j_g L j_e; m_g \Delta m_e) \times \frac{\sigma_0\, f_{LM}\,\chi\,\Gamma}{E_{in}-(E_{m_e}-E_{m_g})+i\Gamma/2}\begin{bmatrix} 1 & 0 \\ 0 & 1 \end{bmatrix}$$

Remember that the third summation will only contribute for $\Delta = m_e - m_g$.

Again, the scattered wave has the same polarization as the incident one. Consequently, polarization changes can only occur in the presence of hyperfine fields with a well defined orientation.

Remark

At resonance, the elastic nuclear forward scattering amplitude is pure imaginary, as can be seen from Eq. (3.4). The wave scattered by a single nucleus has a phase shift of $-\pi/2$ with respect to the incident wave.

3.2.2 Resonant Forward Scattering by an Ensemble of Nuclei

In the foregoing, the forward scattering of γ-rays by a single nucleus has been treated. In the present, the theory will be extended to elastic forward scattering by an ensemble of nuclei. As mentioned before, scattering by an ensemble of nuclei is a collective process. The scattered waves from all nuclei interfere. In this section an expression for the transmitted wave field is derived, taking into account the inter- and intra-nuclear interferences.

When a γ-quantum is transmitted through a target, two independent paths can occur:

- the photon can be transmitted without interaction with the target,
- or, it can be coherently forward-scattered.

According to quantum mechanics, these two paths should be added. Moreover, since both paths are coherent, they should be added on the level of amplitudes instead of intensities.

The wave fields transmitted through the target can thus be written as a coherent superposition of the incident and the forward-scattered wave fields:

$$A_{tr}(\omega) = A_{in}(\omega) + A_{sc}(\omega) \tag{3.5}$$

The incoming and transmitted wave fields are connected via

$$\begin{bmatrix} A^{+}_{tr}(\omega) \\ \\ A^{-}_{tr}(\omega) \end{bmatrix} = S \begin{bmatrix} A^{+}_{in}(\omega) \\ \\ A^{-}_{in}(\omega) \end{bmatrix} \tag{3.6}$$

where the superscripts $+$ and $-$ refer to wave fields with right- and left-handed circular polarization, respectively. An explicit formula for the matrix S is derived in Ref. [52] and reads:

$$S = \begin{bmatrix} \frac{1}{2}\left(e^{\nu d} + e^{\mu d}\right) + \frac{f^{++} - f^{--}}{2\sqrt{}}\left(e^{\nu d} - e^{\mu d}\right) & \frac{f^{-+}}{\sqrt{}}\left(e^{\nu d} - e^{\mu d}\right) \\ \\ \frac{f^{+-}}{\sqrt{}}\left(e^{\nu d} - e^{\mu d}\right) & \frac{1}{2}\left(e^{\nu d} + e^{\mu d}\right) - \frac{f^{++} - f^{--}}{2\sqrt{}}\left(e^{\nu d} - e^{\mu d}\right) \end{bmatrix} \tag{3.7}$$

The argument of the scattering amplitudes has been omitted, for the purpose of brevity. In Eq. (3.7) d is the sample thickness. The symbols μ, ν and $\surd$ are defined by:

$$\mu = \frac{-i\lambda n}{2}\left(f^{++} + f^{--} + \surd\right)$$

$$\nu = \frac{-i\lambda n}{2}\left(f^{++} + f^{--} - \surd\right)$$

$$\surd = \sqrt{(f^{++} - f^{--})^2 + 4f^{+-}f^{-+}}$$

where λ is the wave length of the incident radiation ($\lambda = \frac{2\pi c}{\omega}$) and n is the concentration of the chemical element.

The factor $-i$ in the exponents originates from the integration over all waves diffracted at nuclei in a plane perpendicular to the photon propagation direction. As follows from the Fresnel-Kirchhoff diffraction formula [53], this integration introduces a phase shift of $-\pi/2$ of the diffracted wave with respect to the primary wave at the diffraction plane. At resonance, $f^{\sigma_{in}\sigma_{sc}}(\omega)$ gives an additional phase shift of $-\pi/2$ so that the wave field scattered by an ensemble of nuclei is in exact anti-phase with respect to the incident wave field.

The non-diagonal terms in the S-matrix describe forward scattering processes in which the circular polarization changes. As before, these terms become zero for certain geometries of the hyperfine field. Then, the expression for S takes a very simple form.
For example, if the investigated sample is a single-line, or submitted to randomly oriented hyperfine fields, the scattering matrix S becomes diagonal:

$$S = e^{-i\lambda n d f^{++}} \begin{bmatrix} 1 & 0 \\ 0 & 1 \end{bmatrix} \tag{3.8}$$

3.2.3 TISRS Intensity

For TISRS measurements, a single-line reference sample is placed after the investigated sample. To account for this, the expression (3.6) for the transmitted wave field is adapted according to:

$$\begin{bmatrix} A_{tr}^{+}(\omega) \\ \\ A_{tr}^{-}(\omega) \end{bmatrix} = R\,S \begin{bmatrix} A_{in}^{+}(\omega) \\ \\ A_{in}^{-}(\omega) \end{bmatrix} \tag{3.9}$$

where R is the diagonal matrix for a single-line as given by Eq. (3.8). Of course, n and d should be replaced by the concentration and the thickness of the reference sample.

In the previous expressions, the circular polarization representation of the photon is used rather than the linear representation, because it is easier to express the scattering amplitudes in the former representation. However, since the synchrotron radiation is strongly linearly polarized, it is useful to transform from one representation to the other. This is achieved by the following transformations:

$$\begin{bmatrix} A^{+}(\omega) \\ \\ A^{-}(\omega) \end{bmatrix} = \frac{1}{\sqrt{2}} \begin{bmatrix} -1 & -i \\ \\ 1 & -i \end{bmatrix} \begin{bmatrix} A^{x}(\omega) \\ \\ A^{y}(\omega) \end{bmatrix} = U \begin{bmatrix} A^{x}(\omega) \\ \\ A^{y}(\omega) \end{bmatrix}$$

$$\begin{bmatrix} A^{x}(\omega) \\ \\ A^{y}(\omega) \end{bmatrix} = \frac{1}{\sqrt{2}} \begin{bmatrix} -1 & 1 \\ \\ i & i \end{bmatrix} \begin{bmatrix} A^{+}(\omega) \\ \\ A^{-}(\omega) \end{bmatrix} = U^{-1} \begin{bmatrix} A^{+}(\omega) \\ \\ A^{-}(\omega) \end{bmatrix}$$

Inserting these formulae into Eq. (3.9), yields the following expression for the transmitted wave field in a TISRS measurement with synchrotron radiation:

$$\begin{bmatrix} A_{tr}^{x}(\omega) \\ \\ A_{tr}^{y}(\omega) \end{bmatrix} = U^{-1}\,R\,S\,U \begin{bmatrix} A_{in}^{x}(\omega) \\ \\ A_{in}^{y}(\omega) \end{bmatrix} \tag{3.10}$$

When the reference sample is mounted on a Mössbauer drive, so that the nuclear transition energy is Doppler shifted according to:

$$E(v) = (E_{j_e} - E_{j_g}) \left(1 + \frac{v}{c}\right)$$

then the elastic nuclear forward scattering amplitude for the reference is given by:

$$f^{++}(\omega, v) = -\frac{k_{in}}{8\pi}\,\sigma_0\, f_{LM}\,\chi\,\frac{\Gamma}{E_{in} - E(v) + i\Gamma/2}$$

(Note that $f^{+-} = f^{-+} = 0$ because the reference is a single-line.) This amplitude is not only a function of the energy of the incident radiation, but also of the velocity of the reference sample with respect to the investigated sample.

What is detected in a TISRS measurement, is the time-integrated intensity of transmitted radiation. This one is given by:

$$I_{tr}(v) = \int_0^{+\infty} I_{tr}(t)\,dt \;= \int_0^{+\infty} \left(|A_{tr}^x(t)|^2 + |A_{tr}^y(t)|^2\right)\,dt$$

Or, using Parseval's theorem,

$$I_{tr}(v) = \frac{1}{2\pi}\int_{-\infty}^{+\infty} \left(|A_{tr}^x(\omega)|^2 + |A_{tr}^y(\omega)|^2\right)\,d\omega \tag{3.11}$$

where $A_{tr}^x(\omega)$ and $A_{tr}^y(\omega)$ are the solutions of Eq. (3.10). Via the R-matrix, they are dependent on the velocity of the reference sample. Thus, also the time-integrated intensity will have a velocity dependence.

If a truly time-integrated measurement is performed, the prompt incident radiation as well as the delayed scattered radiation are detected, and Eq. (3.11) gives the measured intensity. However, in most experiments the prompt pulse, at t = 0, is gated because it would only saturate the detector and does not contain any information on the sample. In that case, only forward-scattered intensity is recorded and Eq. (3.11) should be combined with Eq. (3.5) in order to obtain an expression for the forward-scattered intensity. Here, it is assumed that the gate is infinitely short and only t = 0 is cut off. In a real experiment this is unrealistic; the gate will be several ns long. Then, the integration over time is incomplete and expression (3.11) is not valid anymore. This problem, and its consequences for TISRS measurements, are discussed at length in the next chapter. But first, some simulations for the forward-scattered radiation in a fully time-integrated measurement are presented.

3.3 Simulations

As an example, consider the magnetic dipole transition between the ground state and the first excited state of ^{57}Fe. Table 3.1 lists the relevant parameters for this transition.

Table 3.1: Parameters of α-^{57}Fe.

parameter	ground state	1st excited state
nuclear spin	1/2	3/2
quadrupole moment	0	0.082 b [54]
g-factor	0.1812	-0.1033
linewidth	—	4.651 neV
transition energy	14.413 keV	
transition frequency	2.1896 10^{19} Hz	
internal conversion	8.19	
natural abundance	2.19 %	
f_{LM} at RT	0.771	
concentr. of nuclei	8.4603 10^{28}/m^3	

The investigated sample can be a single-line or a hyperfine-split sample, enriched of ^{57}Fe. The reference sample should be a single-line, containing ^{57}Fe, e.g., a stainless-steel absorber.

One introduces the effective resonance thickness, T_{eff}, which combines all relevant parameters of the absorber, via:

$$T_{\text{eff}} = \sigma_0 \; f_{LM} \; \chi \; n \; d$$

It is a measure for the effective number of nuclei participating in the resonant scattering process.

Furtheron, some TISRS simulations for ^{57}Fe are presented for different geometries.

3.3.1 Single-Line

First of all, the investigated sample, as well as the reference are taken as single-line. In this case, the formula for the transmitted wave field becomes very simple:

$$\begin{bmatrix} A_{tr}^{x}(\omega) \\ A_{tr}^{y}(\omega) \end{bmatrix} = e^{-i\frac{T_{\mathrm{eff}}^{r}}{4}\frac{\Gamma}{E_{in}-E(v)+i\Gamma/2}} \; e^{-i\frac{T_{\mathrm{eff}}^{s}}{4}\frac{\Gamma}{E_{in}-(E_{j_e}-E_{j_g})+i\Gamma/2}} \begin{bmatrix} A_{in}^{x}(\omega) \\ A_{in}^{y}(\omega) \end{bmatrix}$$

Here, the definition for the effective resonance thickness of sample (s) and reference (r) has been used.

Figure 3.4 shows the transmitted intensity through both sample and reference as a function of the reference's velocity. A peak appears when the investigated sample and the reference are in resonance. Since no isomer shift has been assumed of the reference with respect to the investigated sample, this peak appears at v = 0 mm/s.

In figure 3.4 two sample thicknesses are simulated. By comparing the left spectrum ($T_{\mathrm{eff}} = 0.5$) with the right one ($T_{\mathrm{eff}} = 7.5$), one immediately notices a difference. For the thin samples, the spectrum shows a nice Lorentz line, while in case of the thicker absorbers, the resonance line is appreciably broadened. This line-broadening, also known in conventional Mössbauer spectroscopy, is the Fourier analogue of speedup in time differential measurements.

As has been shown in Ref. [55], the peak-to-baseline ratio for two single-line absorbers is maximal when the effective thickness of sample and reference are equal.

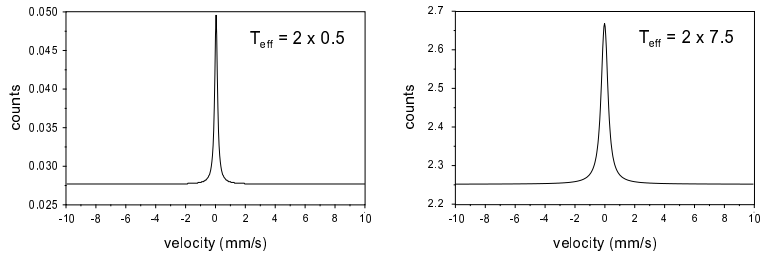

Figure 3.4: Simulation of the TISRS spectrum for two stainless-steel absorbers. Left: The effective thickness of both absorbers is 0.5 ; Right: The effective thickness of both absorbers is 7.5.

3.3.2 Magnetic Interaction

The discussion on TISRS with hyperfine fields will be limited to the magnetic interaction. The electric quadrupole interaction or combined interactions can be treated in a similar way.

If the investigated sample is submitted to a magnetic field, the nuclear levels will show Zeeman splitting and the TISRS spectrum will show several resonances. The number of lines depends on the orientation of the magnetic field with respect to the photon beam and the linear polarization plane.

If the radiation axis system is defined as follows:

- z-axis parallel to the photon beam
- x-axis in the plane of the synchrotron and
  parallel to the electric polarization vector
- y-axis perpendicular to the plane of the synchrotron and
  parallel to the magnetic polarization vector

then (x,y,z) define a right-handed axis system.

The direction of the magnetic field with respect to the radiation axis system is defined by the spherical angular coordinates (θ,φ), as shown in figure 3.5.

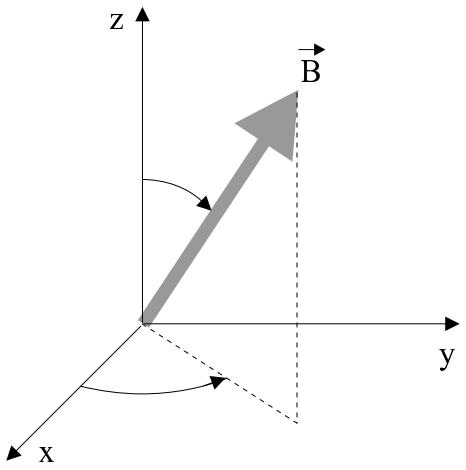

Figure 3.5: Parametrization of the magnetic field direction $\vec{B}$ with respect to the radiation axis system.

For a magnetic dipole transition ($L = 1$ and $\Lambda = 0$) between the nuclear levels, the elastic nuclear forward scattering amplitude is

$$f^{\sigma_{in}\,\sigma_{sc}}(\omega) = \frac{k_{in}}{8\pi}\,\frac{3}{4}\,\sigma_0\, f_{LM}\,\chi\,\sigma_{in}\,\sigma_{sc}$$
$$\times \sum_{m_g}\sum_{m_e}\sum_{\Delta=0,\pm1} C^2(\tfrac{1}{2}1\tfrac{3}{2}; m_g\Delta m_e)\,\mathcal{D}^{(1)*}_{\sigma_{in}\Delta}(\varphi\,\theta\,0)\,\mathcal{D}^{(1)}_{\sigma_{sc}\Delta}(\varphi\,\theta\,0)$$
$$\times \frac{\Gamma}{E_{in} - (E_{m_e} - E_{m_g}) + i\Gamma/2} \qquad (3.12)$$

Depending on the values for (θ,ϕ), the TISRS spectrum will show 2, 4 or 6 lines. The relative intensity of each line depends on the Clebsch-Gordan coefficients and on the rotation matrices. They are listed in table 3.2 and table 3.3, respectively.

Table 3.2: Clebsch-Gordan coefficients $C(\frac{1}{2}1\frac{3}{2}; m_g\Delta m_e)$.

Δ \ m_e	3/2	1/2	- 1/2	- 3/2
+1	1	$\sqrt{1/3}$	0	0
0	0	$\sqrt{2/3}$	$\sqrt{2/3}$	0
-1	0	0	$\sqrt{1/3}$	1

Table 3.3: Product of the rotation matrices for a dipole transition $\mathcal{D}^{(1)*}_{\sigma_{in}\Delta}(\varphi\,\theta\,0)\;\mathcal{D}^{(1)}_{\sigma_{sc}\Delta}(\varphi\,\theta\,0)$.

Δ \ $\sigma_{in}\sigma_{sc}$	$++$	$--$	$+-$	$-+$
+1	$\left(\frac{1+\cos\theta}{2}\right)^2$	$\left(\frac{1-\cos\theta}{2}\right)^2$	$\frac{1}{4}\sin^2\theta\, e^{2i\varphi}$	$\frac{1}{4}\sin^2\theta\, e^{-2i\varphi}$
0	$\frac{1}{2}\sin^2\theta$	$\frac{1}{2}\sin^2\theta$	$-\frac{1}{2}\sin^2\theta\, e^{2i\varphi}$	$-\frac{1}{2}\sin^2\theta\, e^{-2i\varphi}$
-1	$\left(\frac{1-\cos\theta}{2}\right)^2$	$\left(\frac{1+\cos\theta}{2}\right)^2$	$\frac{1}{4}\sin^2\theta\, e^{2i\varphi}$	$\frac{1}{4}\sin^2\theta\, e^{-2i\varphi}$

$\underline{\vec{B} \parallel z}$ $(\theta = 0°)$

If the magnetic field is parallel to the photon propagation direction, only $\Delta = \pm 1$ transitions are excited, as can be seen from table 3.3 by inserting $\theta = 0°$. Moreover, only transitions without circular polarization change occur. The spectrum shows four resonance lines, as illustrated in figure 3.6.

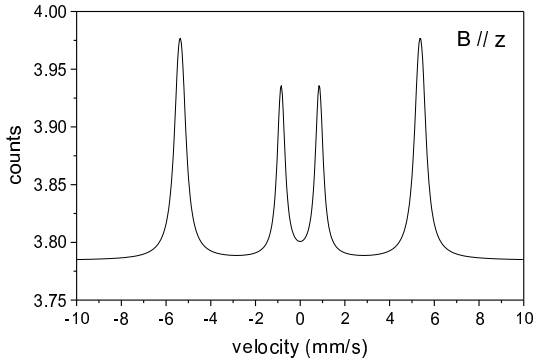

Figure 3.6: TISRS spectrum for a ^{57}Fe sample ($T_{eff} = 20$) in combination with a stainless-steel reference ($T_{eff} = 4$). The investigated sample is submitted to a hyperfine magnetic field of 33.3 T along the z-axis.

$\underline{\vec{B} \perp z}$ $(\theta = 90°)$

When the magnetic field is perpendicular to the photon beam, then, from table 3.3, all Δ transitions are possible and one would expect six lines. However, this will not always be the case for nuclear resonant scattering using synchrotron radiation. Because the incident radiation is linearly polarized, the TISRS spectrum will also depend on the orientation of the hyperfine field with respect to the electric polarization vector. See figure 3.7.

If the magnetic field is parallel to the electric polarization vector ($\varphi = 0°$), then again, only $\Delta = \pm 1$ transitions are allowed. Whereas, if the magnetic field is perpendicular to the electric polarization vector ($\varphi = 90°$), then only $\Delta = 0$ transitions are excited. The spectrum shows two lines of equal intensity.

As the field turns from the x-direction ($\varphi = 0°$) to the y-direction ($\varphi = 90°$) the spectrum gradually changes from four lines ($\Delta = \pm 1$) to two lines ($\Delta = 0$). For the orientation $\varphi = 45°$, one gets maximal intensity for the six lines.

Figure 3.7 shows that the nuclear scattering of synchrotron radiation is sensitive to the direction of the hyperfine fields, even in the plane perpendicular to the photon beam. One can distinguish between $B \parallel x$ and $B \parallel y$. This is an important difference with conventional Mössbauer spectroscopy where unpolarized light is used. There, all orientations of the magnetic field perpendicular to the photon direction would yield identical spectra. The intensity of the resonance lines is then completely determined by the product of Clebsch-Gordan coefficients and rotation matrices. So, in conventional Mössbauer spectroscopy the intensity ratio equals 3:0:1:1:0:3 for the magnetic field along the photon propagation direction and 3:4:1:1:4:3 for the magnetic field perpendicular to this direction. When linearly polarized synchrotron radiation is used, the intensity of each resonance line is calculated, taking into account also the transformation to a linear polarization base.

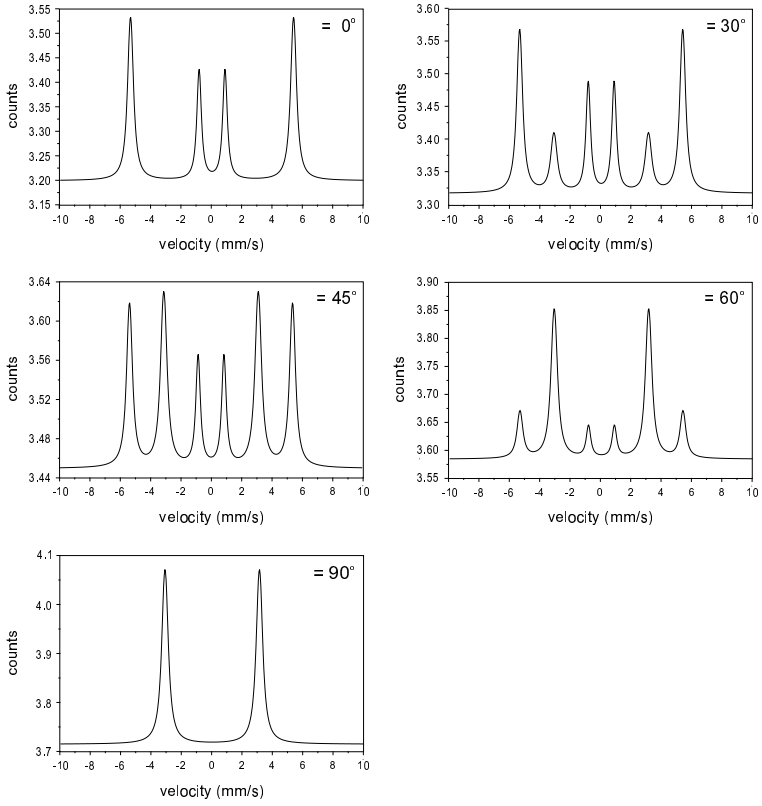

Figure 3.7: TISRS spectrum for a ^{57}Fe sample ($T_{eff} = 20$) in combination with a stainless-steel reference ($T_{eff} = 4$). The investigated sample is submitted to a hyperfine magnetic field of 33.3 T perpendicular to the photon beam.

Chapter 4

TISRS with Time Slicing

In order to test the TISRS technique, a first experiment was performed on two stainless-steel samples. The aim was to register only radiation that had been scattered on the samples. However, in a fully time-integrated measurement, also the incident prompt radiation will be registered. This prompt X-ray burst does not contain any information on the samples. It will only contribute to the background. But, what is worse, it is extremely intense radiation ($> 10^7$ photons/s) and it will saturate the detector for quite some time. For that reason, a gate was used to inhibit detection during the first 20 - 50 ns.

The present chapter reports the results of this experiment. They clearly show the influence of time slicing in time-integrated synchrotron-radiation spectroscopy. The spectra do not have the single-line shape as simulated in the previous chapter. Instead, a complicated oscillatory behavior is seen.

In the second part of this chapter, time slicing in TISRS is discussed and compared to time slicing in Mössbauer spectroscopy. As will be shown, conventional Mössbauer spectra are not so sensitive to the time window. This is explained by a different time dependence of the detected radiation in both techniques.

4.1 Experiment with Time Slicing

4.1.1 Experimental Setup

A schematic overview of the experiment is shown in figure 4.1.

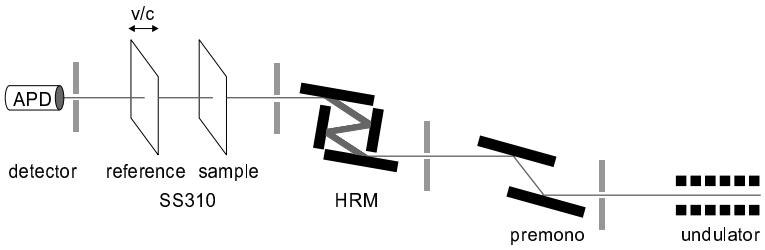

Figure 4.1: Experimental setup for TISRS with time slicing. The propagation direction of the beam is from right to left.

The photon beam is generated by an undulator, tuned to the 14.413 keV nuclear resonance of ^{57}Fe. With a high-heat-load premonochromator, an energy bandwidth of 3.5 eV around resonance is selected. This bandwidth is further reduced by a high resolution monochromator (HRM) to 5.5 meV (cf. chapter 2). Next, the synchrotron beam interacts with two samples. Both are 42% enriched stainless-steel SS310 at room temperature, with an effective thickness of 9. One of them, the reference sample, is mounted on a Mössbauer drive whose velocity changes sinusoidally. The other sample is kept stationary. The radiation scattered by the samples in forward direction is recorded by an avalanche photodiode detector (APD), with an efficiency of 20%.

During this experiment, the APS storage ring was filled with doublets, giving two pulses every 100.8 ns. The distance between the two doublet pulses is 2.8 ns. For stability reasons, however, the ring is not filled symmetrically. At one point on the circumference there is a larger sequence of successive bunches (e.g., twelve pulses separated by 2.8 ns). This is illustrated in figure 4.2.

The prompt count rate after the HRM was 10^7 Hz at 100 mA electrons stored in the ring. In order to avoid saturation of the electronics due to the prompt radiation, forward-scattered photons are only registered within a certain time window after each doublet.

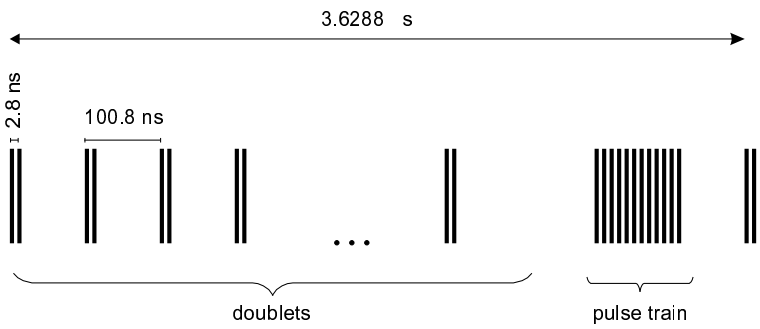

Figure 4.2: Filling scheme of the APS storage ring.

4.1.2 Electronics Setup

Figure 4.3 shows the electronics arrangement for TISRS measurements with time slicing. It consists of an anticoincidence circuit for the timing and an additional circuit for the velocity dependent measurements.

For the anticoincidence, the output pulse of the detector is split by a constant-fraction discriminator (CFD1). One output goes to the prompt count rate meter. The other output is fed into a logic unit (LOG). On the other hand, the bunch clock signal of APS (BC) also passes through a constant-fraction discriminator (CFD2), where it is shaped and split into two output signals. The shape of the pulse is adjusted so that its width matches the length of the desired time gate. One output is μs-delayed by means of cables. This long delay is necessary because the storage ring is not filled symmetrically (see figure 4.2). Then, the signal is processed by a ns-delay module in order to synchronize the bunch clock signal to the detector signal. Finally, the delayed signal is fed into the logic unit (LOG). Both inputs, the one coming from the detector and the one coming from the bunch clock, are set in anticoincidence. Thus, there is only an output for photons reaching the detector outside the gated time window. This output pulse serves as start for the time-to-amplitude converter (TAC). The stop is supplied by the APS bunch clock signal. The TAC is connected via an analog-to-digital converter (ADC) to a multi-channel analyzer (MCA1), which records the time differential spectrum. From the logic unit (LOG) another output goes to the delayed count rate meter.

For the Mössbauer energy spectrum, a third output of the logic unit is fed into a second multi-channel analyzer (MCA2), which is also connected to the function generator (FG) controlling the Mössbauer drive unit (MDU). MCA2 operates in multi-channel scaling mode and yields a velocity dependent spectrum.

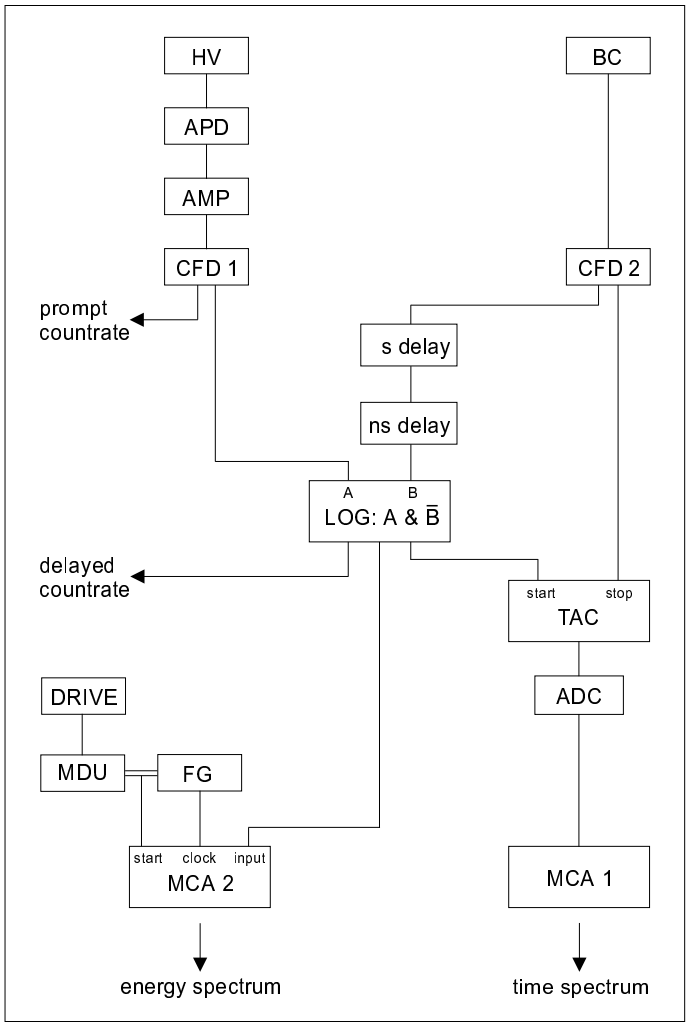

Figure 4.3: Electronics scheme for TISRS measurements at APS. BC: bunch clock of APS; HV: high-voltage supply; APD: avalanche photodiode detector; AMP: amplifier; CFD1, CFD2: constant-fraction discriminator; LOG: 4-input logic unit; TAC: time-to-amplitude converter; ADC: analog-to-digital converter; MCA1, MCA2: multi-channel analyzer; FG: function generator; MDU: Mössbauer drive unit.

4.1.3 Results

Figure 4.4 shows the TISRS spectra recorded in four different time windows. The indicated times refer to the time elapsed after the arrival of the first pulse of the doublet. The data collection time varied from 20 to 60 minutes, depending on the delayed count rate.

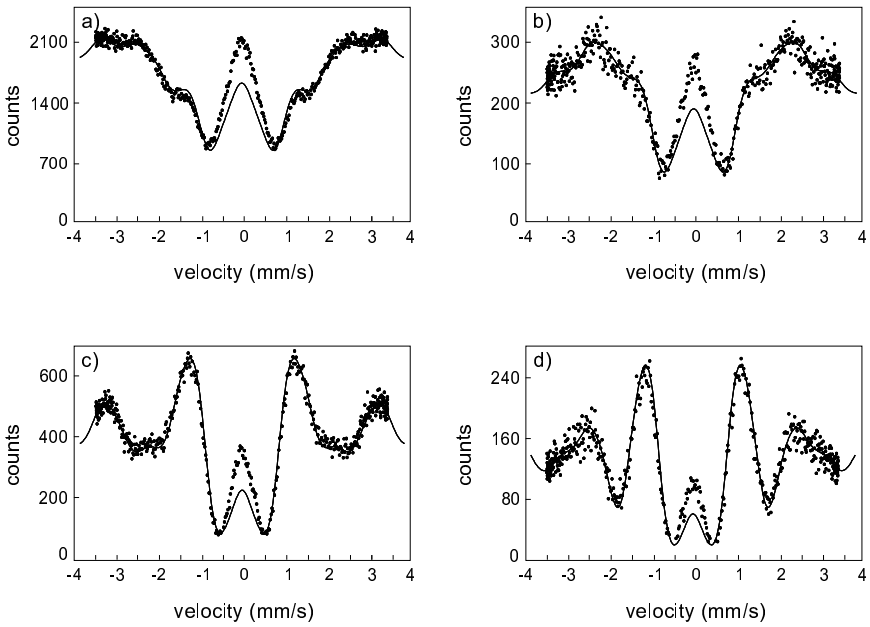

Figure 4.4: TISRS results for different time windows:
a) 22 - 82 ns (data collection time = 55 min at 310 Hz),
b) 27 - 82 ns (data collection time = 60 min at 50 Hz),
c) 47 - 86 ns (data collection time = 30 min at 120 Hz),
d) 58 - 86 ns (data collection time = 20 min at 60 Hz).

From Fourier theory one can expect that time slicing will introduce oscillations in the energy spectrum. This has also been seen in conventional Mössbauer spectroscopy [56], but there the oscillations are not so prominent. In time-integrated synchrotron-radiation spectroscopy, however, the oscillations are much more pronounced and extremely sensitive to the chosen time window, as can be seen in figure 4.4. The influence of the oscillations on the spectrum is dramatic. Instead of having a nice single-line peak at v= 0 mm/s, the spectrum shows a complicated oscillatory behavior. In the next section, we will discuss this point in more detail.

The solid lines in figure 4.4 are simulations based on the semiclassical optical model for radiation, as explained in chapter 3. The calculations are done with the Mathcad program. In appendix A the algorithm is explained and a copy of the program is included.
The qualitative features of the spectra could be reproduced using the parameters mentioned above. However, all simulations show a misfit around zero velocity. In order to solve this problem, several effects have been investigated.

In a first attempt, we have considered a thickness distribution of the samples. Instead of a unique and well defined effective thickness, $T_{eff} = 9$, a Gaussian distribution centered about this value has been assumed. This did not improve the quality of the fit.

Secondly, we have considered the possibility to have coherence between different synchrotron photons. A short calculation learns that in the actual experiment the chances to see intra-pulse coherence are extremely low. Indeed, the probability for having a resonant photon in a particular bunch is determined by the ratio of the delayed count rate to the number of bunches per second, which in this case yields a probability of approximately 10^{-5}. The probability to have two resonant photons is 10^{-10}, which is 10^5 times smaller. So, one can conclude that with a delayed count rate of only 10^2 Hz, it is impossible to see coherence effects between two resonant photons.

Maybe the misfit should be attributed to the fact that the large pulse train (see figure 4.2) gives a contribution to the spectrum which is different from the contributions of the doublets. This could not be included into the simulation because the exact filling mode, i.e. the number of bunches in the pulse train and its position relative to the doublets, were not known.

Finally, another phenomenon that can be considered is the contribution of channels that do not only contain forward scattering. If a photon is scattered by a resonant nucleus, the emitted radiation can either go in forward direction towards the detector, or, it can first be resonantly scattered by a neighboring nucleus before proceeding in forward direction. The interference between the two paths creates a kind of holographic effect that alters the radiation pattern. For thin samples, this second order effect is expected to be small, because it involves a double-scattering event. For thicker samples, the probability for double scattering increases. This might explain why this effect would only contribute at $v = 0$ mm/s, where both absorbers are in resonance, and thus, the effective thickness of the resonance medium is increased.

4.2 Discussion

4.2.1 Sensitivity to Time Slicing

As mentioned in the previous chapter, the time-integrated nuclear forward-scattered intensity is given by

$$\int_0^{+\infty} I_{fs}(t)\, dt$$

where $I_{fs}(t)$ is the forward-scattered intensity as a function of time. When time slicing is applied, the above formula should be replaced by

$$\sum_{i=0}^{\infty} \int_{t_b+i\Delta}^{t_e+i\Delta} I_{fs}(t)\, dt \tag{4.1}$$

The summation is due to the pulsed time structure of the synchrotron radiation. After each pulse, the detector is inhibited during a certain time t_b. The same is true before each pulse, starting from a time t_e. With Δ the time interval between pulses, Eq. (4.1) thus gives the forward-scattered intensity when time gating is repeated periodically around each synchrotron pulse. The incomplete integration over time results in oscillations in the energy spectrum. This is well known from Fourier theory.

The oscillatory behavior changes quickly when the integration range decreases. This is illustrated in the figures 4.5, 4.6 and 4.7. The spectra are simulated for two stainless-steel samples and for a pulse separation of 100 ns. The integration window runs from a variable value t_b, indicated next to each curve, till 100 ns and is repeated periodically for each pulse. The appearance of the spectra changes drastically as the integration window starts at later times.

The difference between the three figures is due to different sample thicknesses. In figure 4.5 the effective thickness of both samples is 4.5, while in figure 4.6 it is 9 and in figure 4.7 it is 18. By comparing, e.g., figure 4.6 with figure 4.7, one immediately sees that the oscillations depend strongly on the effective thickness. When one tries to estimate the maximum allowed time the gate may be closed in order to still recognize the hyperfine splitting, the sample thickness will play a role. For the thin samples (figure 4.5), the tolerable width is ± 10 ns. Cutting off a larger time after the synchrotron pulse distorts the spectra significantly and makes the interpretation difficult. When going to thicker samples, the acceptable time cut gets smaller. For the intermediate sample thickness (figure 4.6) it is 5 ns and for the thick samples (figure 4.7) it is even less. The fact that the tolerable width decreases with increasing sample thickness can be understood from the time response of the three systems, given in figure 4.8. The thicker the absorber,

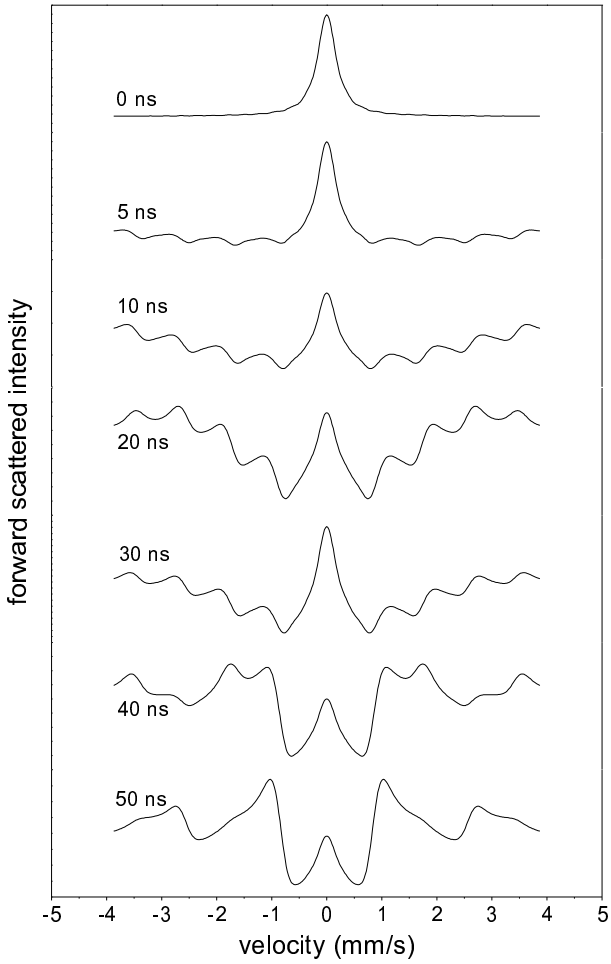

Figure 4.5: Simulated energy spectra for TISRS with time slicing for two stainless-steel samples ($T_{eff} = 2 \times 4.5$). The labels next to each curve indicate the beginning of the integration range after each synchrotron pulse. The pulse separation is 100 ns.

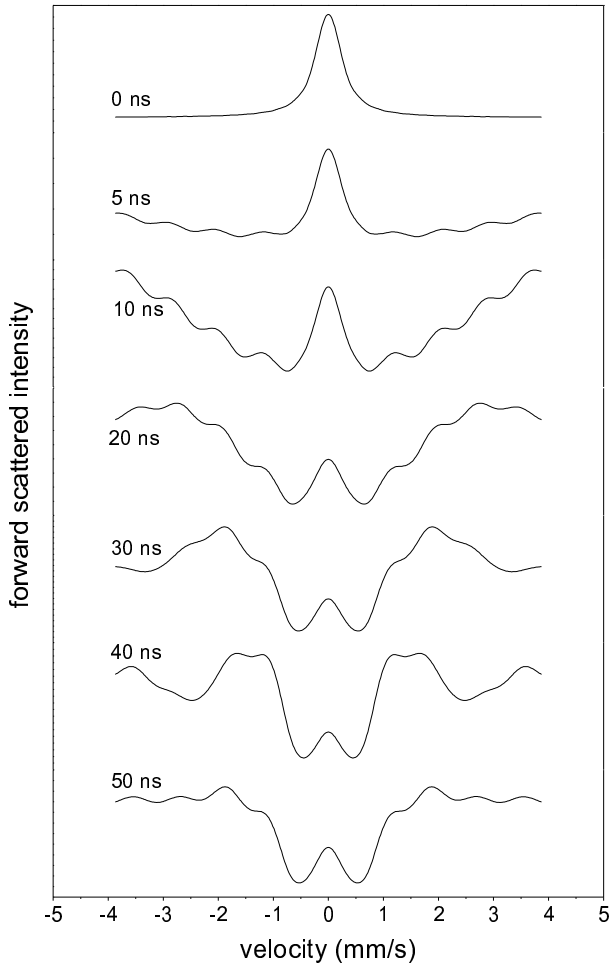

Figure 4.6: Simulated energy spectra for TISRS with time slicing for two stainless-steel samples ($T_{eff} = 2 \times 9$). The labels next to each curve indicate the beginning of the integration range after each synchrotron pulse. The pulse separation is 100 ns.

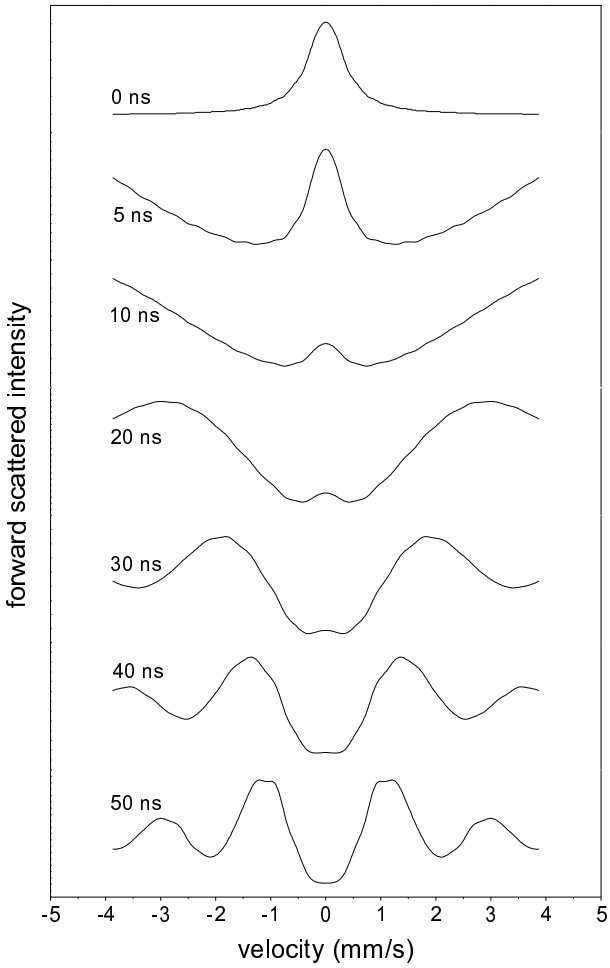

Figure 4.7: Simulated energy spectra for TISRS with time slicing for two stainless-steel samples ($T_{eff} = 2 \times 18$). The labels next to each curve indicate the beginning of the integration range after each synchrotron pulse. The pulse separation is 100 ns.

the stronger the speedup of the resonant scattering and, consequently, the larger the contribution of earlier times to the forward-scattered intensity. Cutting off the beginning of the time response will thus have a larger impact on the resulting energy spectrum. Another aspect that one has to take into account when thick samples are used, is the dynamical beat pattern. For the thick absorbers ($T_{eff} = 2 \times 18$) there are several dynamical minima in the first 300 ns, and the TISRS spectrum will depend on the position of the time window with respect to these minima.

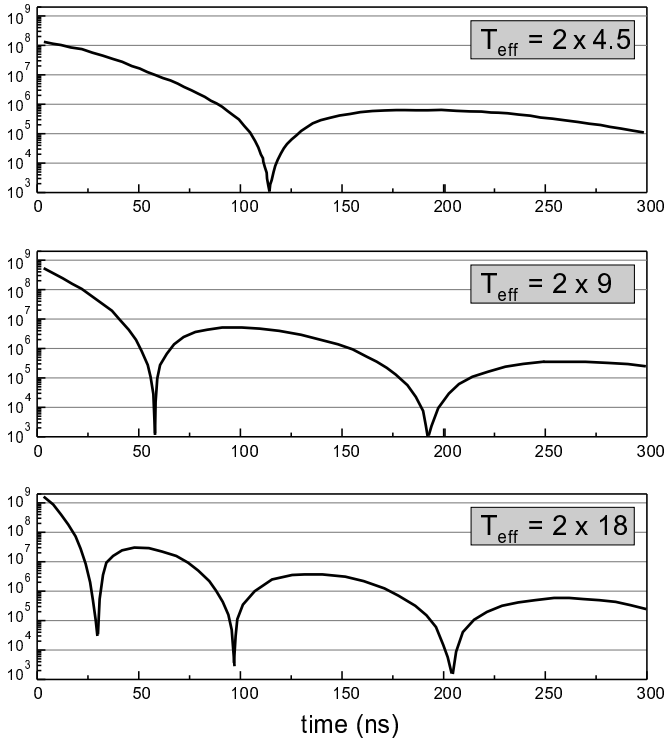

Figure 4.8: Nuclear resonant forward-scattered intensity as a function of time for two stainless-steel samples. Three different sample thicknesses are simulated. (Note that the intensity scale is logarithmic.)

Apart from the effective thickness, also the nuclear lifetime of the excited state and the repetition rate of the synchrotron pulses will be decisive in the determination of the tolerable gating. The nuclear lifetime determines the time scale of the scattering process. If the nuclear lifetime is only 10 ns, it is obvious that cutting off the first 5 ns already alters the spectrum considerably. On the other hand, the synchrotron pulse repetition rate determines the frequency of time slicing. Cutting off 5 ns every 100 ns or every 25 ns will give totally different results.

4.2.2 Comparison with Mössbauer Spectroscopy

In conventional Mössbauer Spectroscopy, the source emits monochromatic radiation ($\Delta E \approx \Gamma$) that is resonantly scattered by nuclei in the absorber. The absorber is moved relative to the source so that the transition frequencies are Doppler shifted. See figure 4.9 a.

An equivalent scheme can be obtained with synchrotron radiation by using a thin nuclear monochromator [57]. The setup is sketched in figure 4.9 b. The incident radiation generated by an undulator is monochromatized down to the level of a few neV by the nuclear monochromator which acts as a Mössbauer source. The radiation is then scattered by a modulated sample containing the same Mössbauer active nuclei as the nuclear monochromator. This synchrotron Mössbauer source emits radiation of about the natural linewidth, but, in contrast to a conventional Mössbauer source, the emitted radiation is highly directed and of pure linear polarization.

Time Dependence of Transmitted Radiation in Mössbauer Spectroscopy

If time slicing is performed in Mössbauer spectroscopy, the spectra look quite different from the ones obtained in the previous time-sliced TISRS measurement. Experimental results of time-sliced Mössbauer spectroscopy [56, 58] are shown in figure 4.10. Similar results for a synchrotron-based experiment are reported in Ref. [59].

In these two cases, time slicing only affects the resonance line: two 'shoulders' appear on the resonance wings. The baseline, i.e. the off-resonance channels, are hardly influenced.
This can be understood easily by investigating the time evolution of the transmitted radiation in a Mössbauer experiment. An analytical expression has been derived in Ref. [60]:

$$I_{tr}(t) = e^{-t/\tau} \left| \sum_{n=0}^{\infty} \left(\frac{i\, 2\, \Delta\omega\, \tau}{T_{\text{eff}}} \right)^n \sqrt{\frac{T_{\text{eff}}\, t}{\tau}}^{\,n} J_n(\sqrt{T_{\text{eff}}\, t/\tau}) \right|^2 \qquad (4.2)$$

In this expression, $J_n(z)$ is the Bessel function of n-th order, which satisfies the differential equation [61]:

$$z^2 \frac{d^2y}{dz^2} + z \frac{dy}{dz} + (z^2 - n^2)\, y = 0$$

a) Mössbauer spectroscopy

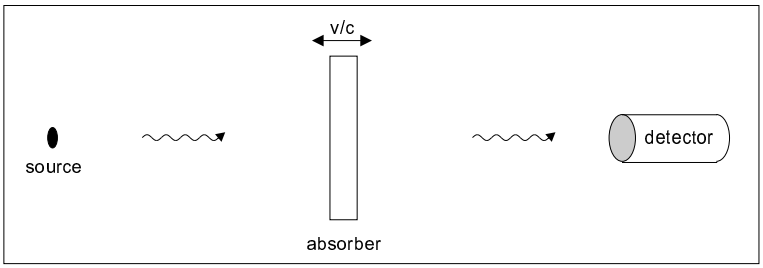

b) Synchrotron-based Mössbauer spectroscopy

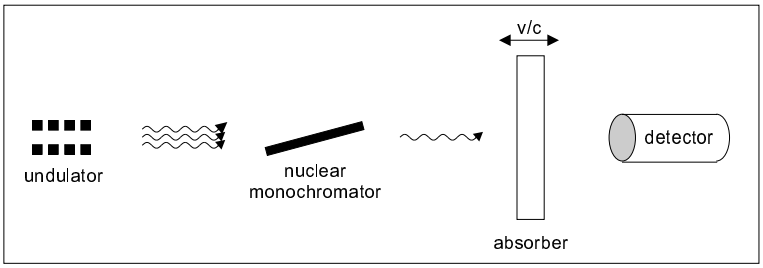

c) Time-integrated synchrotron-radiation spectroscopy

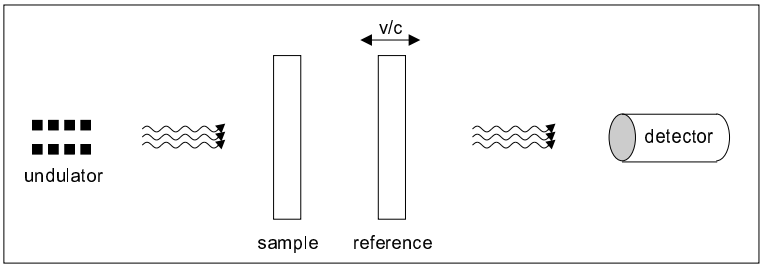

Figure 4.9: Simplified scheme of the setup in:
a) conventional Mössbauer spectroscopy,
b) synchrotron-based Mössbauer spectroscopy,
c) time-integrated synchrotron-radiation spectroscopy.

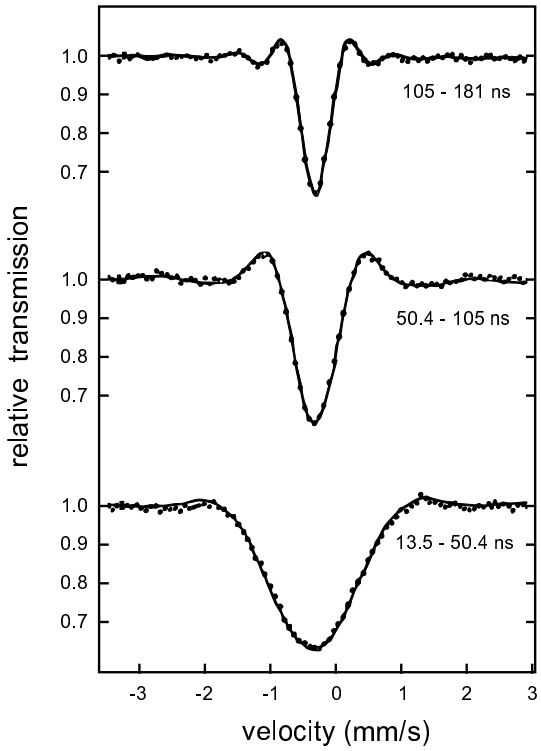

Figure 4.10: Experimental results of time-sliced Mössbauer spectroscopy for a single-line source (^{57}Co in Cu) and a $[Na_4Fe(CN)_6]$-absorber with effective thickness $T_{eff} = 14$ [56]. The solid lines are simulations based on Eq. (4.2).

$\Delta\omega$ is the difference in resonance frequency between the source and absorber nuclei. Its value changes as a function of the absorber's velocity.

Eq. (4.2) is valid when the source and absorber are both single-line. The photoelectric absorption has been neglected. It can be accounted for by multiplying the above expression with $e^{-\sigma_{ph}\, n\, d}$, σ_{ph} being the cross-section for photoelectric absorption. Time $t = 0$ is defined as the instant when the nuclear excited state is formed in the source. In the case of ^{57}Fe, e.g., this moment can be determined experimentally by the emission of a 122 keV gamma in the decay of ^{57}Co.

It has been shown in Ref. [60] that, far away from resonance, the time response approaches the normal exponential decay of an isolated nucleus:

$$I_{tr}(t) \approx e^{-t/\tau}$$

In this region, the time response is independent of $\Delta\omega$ and therefore, the integral over a certain time window will be the same for all velocity channels.

In general, the transmitted intensity, as given by Eq. (4.2), depends on $\Delta\omega$ and thus, on the relative velocity of the absorber. In figure 4.11, the modulus squared which appears in Eq. (4.2) is simulated for several values of $\Delta\omega$, for a stainless-steel absorber with effective thickness 18. As $\Delta\omega$ increases, the simulated function oscillates more and more about 1 and the amplitude of oscillation decreases. For $\Delta\omega = 0.57$ Hz the amplitude is already reduced to 10%. This corresponds to the position in the Mössbauer spectrum $v = 8 \cdot 10^{-9}$ mm/s. The small oscillations about 1 are only relevant on a small time scale (time windows of only a few ns). If, however, longer integration ranges are chosen, as in figure 4.10, the oscillations tend to level out quickly as $\Delta\omega$ increases. Only in the near neighborhood of resonance, the transmitted intensity deviates from a purely exponential decay, and only there, the Mössbauer spectrum will be sensitive to time slicing.

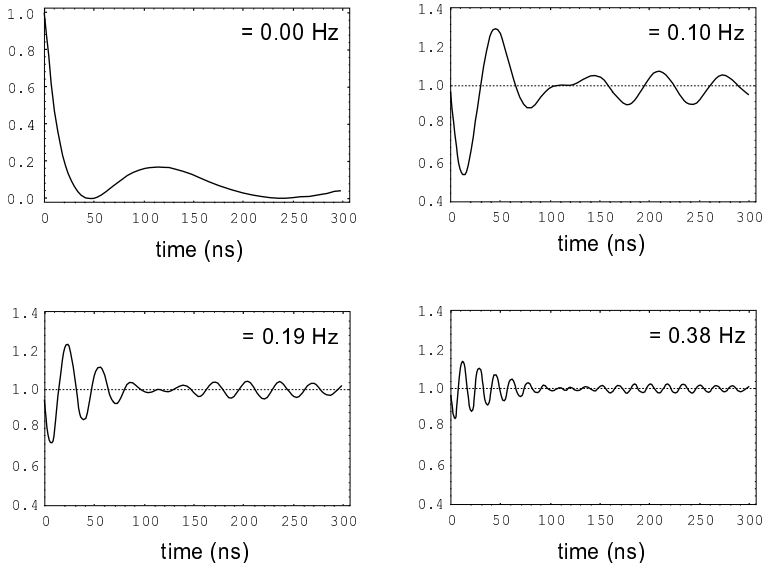

Figure 4.11: Simulations of the time dependence in conventional and synchrotron-based Mössbauer spectroscopy for a stainless-steel absorber with effective thickness $T_{eff} = 18$. The transmitted intensity, divided by $e^{-t/\tau}$, is plotted for four different Doppler shifts between the source and the absorber.

Time Dependence of Scattered Radiation in TISRS

The picture looks very different for TISRS. Now, there are two absorbers that are excited by broadband radiation. See figure 4.9 c. Time $t = 0$ is sharply determined by the arrival of the synchrotron pulse. The time response of a single absorber after excitation by a synchrotron photon was obtained in Ref. [62]:

$$A_{tr}(t) = \frac{\Gamma}{\hbar} \left\{ \delta(t/\tau) - e^{i\,\omega_0\,t - t/2\,\tau}\ \frac{T_{\text{eff}}}{2}\ \frac{J_1(\sqrt{T_{\text{eff}}\,t/\tau})}{\sqrt{T_{\text{eff}}\,t/\tau}} \right\}$$

Again, the photoelectric absorption has been neglected. The delta function describes the prompt, incident radiation, while the second term describes the delayed, scattered radiation. Thus, the forward-scattered wave field as a function of time is given by

$$A_{fs}(t) = \frac{\Gamma}{\hbar}\ \frac{T_{\text{eff}}}{2}\ e^{-t/2\,\tau}\ \left\{ -e^{i\,\omega_0\,t}\ \frac{J_1(\sqrt{T_{\text{eff}}\,t/\tau})}{\sqrt{T_{\text{eff}}\,t/\tau}} \right\}$$

This is the time response for a single absorber. If, as in TISRS, two absorbers are used, an analogous formula holds for the second absorber. The intensity of forward-scattered radiation is obtained by summing both amplitudes and taking the norm squared afterwards. For two absorbers with equal effective thickness, this yields the following expression:

$$I_{fs}(t) = \frac{\Gamma^2}{\hbar^2}\ \frac{T_{\text{eff}}^2}{2}\ e^{-t/\tau}\ \left\{ \left(\frac{J_1(\sqrt{T_{\text{eff}}\,t/\tau})}{\sqrt{T_{\text{eff}}\,t/\tau}} \right)^2 [1 + cos(\Delta\omega\,t)] \right\} \qquad (4.3)$$

The time behavior of the detected radiation in a TISRS experiment, as given by Eq. (4.3), is completely different from the one in a conventional Mössbauer experiment, given by Eq. (4.2). In TISRS, the exponential decay function is multiplied by two time dependent functions (the factors in between the large brackets of Eq. (4.3)). The cosine function describes the quantum beat between the two absorbers, which depends on the relative velocity of the reference sample. The factor $\left(\frac{J_1(\sqrt{T_{\text{eff}}\,t/\tau})}{\sqrt{T_{\text{eff}}\,t/\tau}} \right)^2$ describes the speedup and the dynamical beat in thick absorbers. This function is independent of $\Delta\omega$. So, when $\Delta\omega$ increases, the second factor, $[1 + cos(\Delta\omega\,t)]$, will give much faster oscillations, but the overall envelope, given by the

first factor, remains the same. This can be seen from figure 4.12.
Eq. (4.3) never approaches a purely exponential decay and remains velocity dependent. Therefore, time slicing will influence the TISRS spectrum over the whole velocity range.

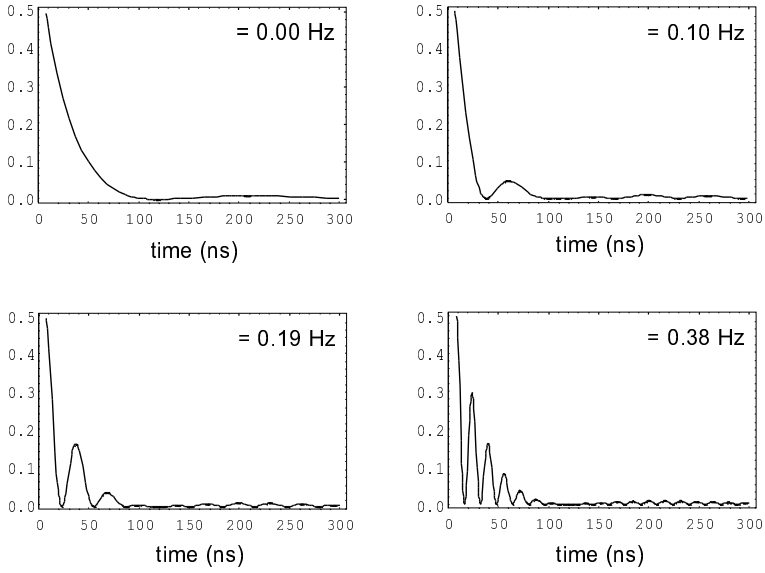

Figure 4.12: Simulations of the time dependence in TISRS for two stainless-steel absorbers with effective thickness $T_{eff} = 18$. The scattered intensity, divided by $\frac{\Gamma^2}{\hbar^2}\frac{T_{eff}^2}{2}e^{-t/\tau}$, is plotted for four different Doppler shifts between the two samples.

Sign of the Resonance

To conclude this section, an additional difference between TISRS and Mössbauer spectroscopy should be addressed. Not only the time dependence is different in both techniques, but also the sign of the resonance. In TISRS the resonance manifests itself as an increased intensity, while in Mössbauer spectroscopy it corresponds to a decrease in transmitted intensity. This can be explained by means of figure 4.13.

In TISRS, the detected intensity arises from an interference between two scattering paths. The main contribution comes from a single scattering on the sample, this is the first path, and a single scattering on the reference, the second path. At resonance, each forward scattering introduces a π phase-shift of the scattered wave field [15]. Consequently, both scattering paths in TISRS are in phase and interfere constructively.

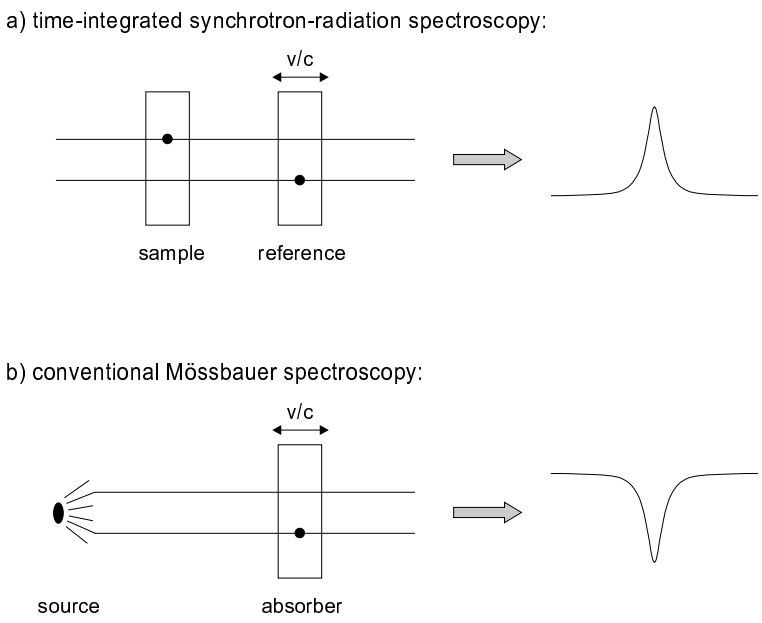

Figure 4.13: Difference between TISRS and Mössbauer spectroscopy.

In a Mössbauer experiment, the main contribution to the detected radiation stems from an interference between the direct path without scattering and the single-scattering path. Both are in anti-phase [63] and thus, the interference will be destructive.

4.3 Conclusion

Unlike Mössbauer spectroscopy, time slicing in TISRS distorts the spectra significantly. The on-line interpretation in terms of hyperfine splittings is hindered by strong oscillations, originating from the incomplete integration over time. To obtain spectra that can be easily interpreted, the allowed inhibition time for the detection after each synchrotron pulse is very short (typically less than 5 ns). This implies that the actual setup with a high-resolution monochromator is not suited for time-integrated synchrotron-radiation spectroscopy. The prompt intensity after the HRM is too high for the detector system and dead times of several tens of ns are common.

If TISRS is to become a useful hyperfine technique, other setups have to be thought of, where the prompt count rate can be reduced to an amount acceptable by the detector. An example is to use a crossed polarizer and analyzer. This setup and its application in TISRS measurements are discussed in the next chapter. Other possible solutions are presented in chapter 6.

Chapter 5

TISRS with Crossed Polarizer and Analyzer

In the present chapter, a second measurement is reported, also performed at the 3ID-undulator beamline at APS [64]. In this experiment, time slicing was reduced to a minimum by using a crossed polarizer and analyzer. These crystals select the resonant part from the broadband spectrum of incident radiation. The nonresonant radiation is strongly suppressed. As a result, the detector system does not get overloaded by the prompt synchrotron burst, and fully time-integrated measurements can be done.

In the first section, the crossed polarizer and analyzer are implemented in TISRS. The theory for time-integrated nuclear resonant forward scattering of synchrotron radiation is adapted in order to include the polarizer and analyzer crystals.
The next section describes the experiment. The obtained TISRS spectrum does not suffer anymore from time slicing, and could be reproduced nicely by the simulations.
The results for TISRS and TDSRS are compared and the advantages and disadvantages of the time-integrated technique are pointed out. Finally, the use of the polarizer and analyzer will be addressed. As will be discussed, the application of the polarizer and analyzer in TISRS is unfavorable from a statistical point of view, but, on the other hand, it has the advantage that the nonresonant intensity is reduced substantially.

5.1 Implementation of the Crossed Polarizer and Analyzer in TISRS

In order to overcome the problem that the detector gets saturated by the prompt synchrotron burst and to avoid the consequences of time slicing, a polarizer and analyzer are integrated in the TISRS setup. The two samples, the investigated one and the reference, are placed between the polarizer and analyzer crystals. The detector comes after the analyzer.
The polarizer transmits σ-polarized radiation, while the analyzer selects π-polarized light. Thus, only radiation that changes its polarization state from σ to π can reach the detector. This may occur for the resonant radiation when it is scattered on a hyperfine-split sample. The nonresonant prompt radiation remains σ-polarized and is reduced by the analyzer by a factor of $6 \cdot 10^{-7}$ (cf. chapter 2). In this way, saturation of the detector is avoided and fully time-integrated measurements can be performed.

The scattering scheme for TISRS with polarizer and analyzer looks somehow different from the one explained before. Since the reference is always a single-line, it cannot introduce polarization changes. This has been pointed out in chapter 3. So, the radiation should have been scattered on the investigated sample in order to pass the analyzer. The main contribution to the detected intensity is an interference between a single-scattering path (only scattering on the investigated sample) and a double-scattering path (scattering on both samples). This is illustrated in figure 5.1. Both amplitudes are in antiphase and, hence, interfere destructively on resonance. Therefore, the resonance lines in the TISRS spectrum will appear as dips instead of peaks [28].

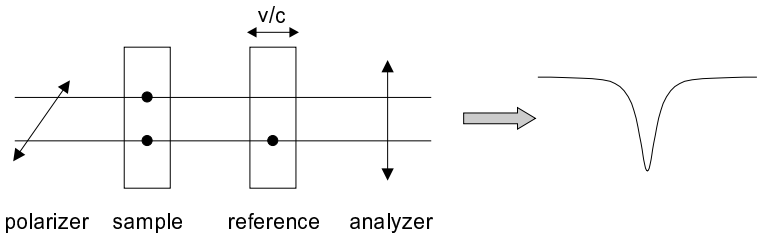

Figure 5.1: Scattering scheme for TISRS with crossed polarizer and analyzer.

The theory for TISRS, as described in chapter 3, can easily be adapted so as to include the polarizer and analyzer crystals. The polarizer and analyzer can be described by the 2×2 matrices P_x and P_y, respectively:

$$P_x = \begin{bmatrix} 1 & 0 \\ 0 & 0 \end{bmatrix} \qquad P_y = \begin{bmatrix} 0 & 0 \\ 0 & 1 \end{bmatrix}$$

Inserting these matrices into Eq. (3.10), the amplitudes of transmitted radiation in TISRS with polarizer and analyzer are given by:

$$\begin{bmatrix} A^x_{tr}(\omega) \\ \\ A^y_{tr}(\omega) \end{bmatrix} = P_y\, U^{-1}\, R\, S\, U\, P_x \begin{bmatrix} A^x_{in}(\omega) \\ \\ A^y_{in}(\omega) \end{bmatrix} \tag{5.1}$$

P_x selects the x-component of the incoming radiation. This is the component with σ-polarization. P_y selects the y-component of the scattered radiation (corresponding to π-polarization). From Eq. (5.1), the transmitted and forward-scattered intensity can be calculated, similar as in section 3.2.

In figure 5.2 simulations for the forward-scattered TISRS intensity with and without polarizer/analyzer are shown. By comparing both figures, one immediately notices the differences: first of all, the sign of the resonances is inverted. Secondly, the relative intensity of the six lines is different. By adding a crossed polarizer and analyzer to TISRS, the amplitude of a particular line in the energy spectrum is altered according to the amount of polarization change for that transition.

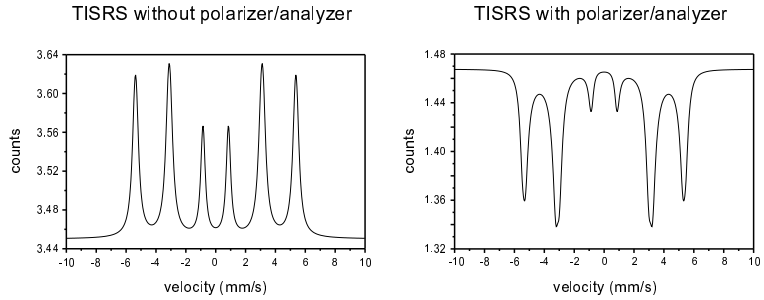

Figure 5.2: TISRS simulations for a Fe sample ($T_{eff} = 20$) in combination with a stainless-steel reference ($T_{eff} = 4$). The investigated sample is submitted to a hyperfine magnetic field of 33.3 T, perpendicular to the photon beam and under an angle of 45° with respect to the linear polarization direction of the incident radiation.

5.2 Experiment with Polarizer/Analyzer

5.2.1 Experimental Details

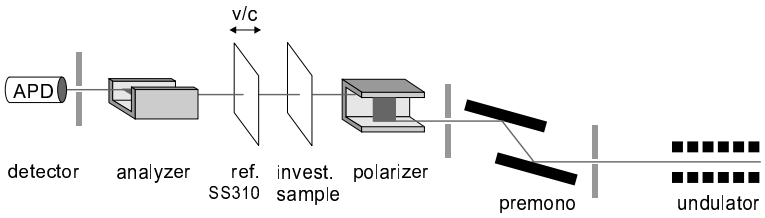

Figure 5.3: Experimental setup for TISRS with crossed polarizer and analyzer. The propagation direction of the beam is from right to left.

An overview of the experimental setup is given in figure 5.3. The undulator is tuned to the 14.413 keV nuclear resonance of ^{57}Fe. With a high-heat-load Si(1 1 1) double crystal monochromator, an energy bandwidth of 3.5 eV at the nuclear resonance is selected. The flux right after the monochromator is 3×10^{13} photons/s. A crossed polarizer and analyzer crystal for the 14.413 keV nuclear resonance of ^{57}Fe [37] are used to reduce the prompt intensity. These consist of two Si(8 4 0) channel-cut crystals in dispersive setting. A detailed description has been given in chapter 2.

Two absorbers at room temperature are placed between the polarizer and the analyzer. The first absorber, the investigated sample, is a magnetically split Fe foil of 2.5 μm thickness, 53% enriched in ^{57}Fe. A small external magnetic field (0.27 $\pm$ 0.03 T) is applied to this sample in order to orient the hyperfine field perpendicular to the beam direction and under an angle of 45° with respect to the linear polarization plane of the synchrotron. This particular direction of the magnetic field gives maximal transmission through the polarizer/analyzer setup [28]. The second absorber is a 2.1 μm thick stainless-steel foil (SS310) with 95% ^{57}Fe enrichment. This one is mounted on a Mössbauer drive in triangular mode, and acts as a single-line reference sample.

The forward-scattered photons are registered by a fast operating avalanche photodiode detector (20% efficiency at 14.413 keV) in intervals of 93 ns, starting from 2 ns after the synchrotron pulse. The electronics setup is analogous to the one described in the previous chapter (section 4.1).
The measurement was performed with a pulse separation of 100 ns (single pulses) and a mean resonant count rate of 40 photons/s. The data collection time was 5 hours.

The nonresonant count rate in this experiment was only 4×10^2 Hz. So, in principle, it was not necessary to put a time gate. However, for background reduction, a very short gate of 2 ns was applied. Simulations in chapter 4 have shown that such a small time cut has negligible effects on the measurement.

Shielding against background becomes a concern when performing measurements with a crossed polarizer and analyzer, since it is necessary to guard against diffuse scattering. The scattering of X-rays on the walls is very small (10^{-6} of the total intensity) but with an incoming flux of 10^{13} Hz, this still gives 10^7 counts per second in the detector. Therefore, lead shielding is done and the beam transport between the different components is accomplished through He-filled cylinders.

5.2.2 Result

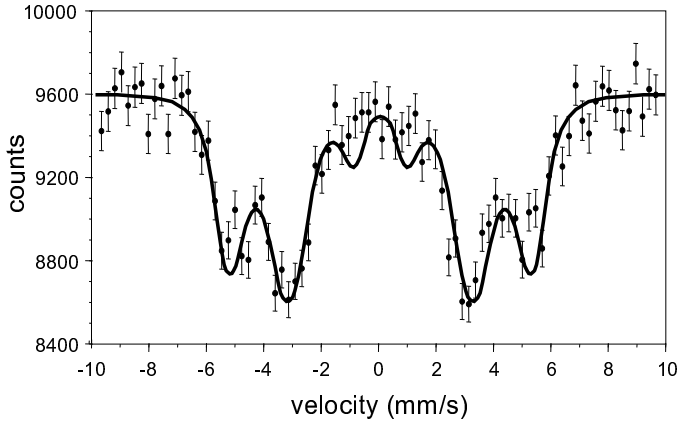

Figure 5.4: TISRS spectrum of a magnetically split Fe sample (T_{eff} = 21) and a stainless-steel reference sample (T_{eff} = 18) in the presence of a crossed polarizer and analyzer. The solid line is the calculated theoretical spectrum.

The resulting time-integrated spectrum is given in figure 5.4, showing the forward-scattered intensity versus the Doppler velocity of the reference sample. The smooth line is a simulation based on the semiclassical optical model for nuclear resonant scattering [13]. The spectrum clearly shows the six ^{57}Fe peaks corresponding to transitions involving an angular momentum change $\Delta = 0, \pm 1$. The separation between the resonances and the relative amplitudes provides information on the hyperfine interactions, while the resonance widths are related to the effective thickness of the samples.

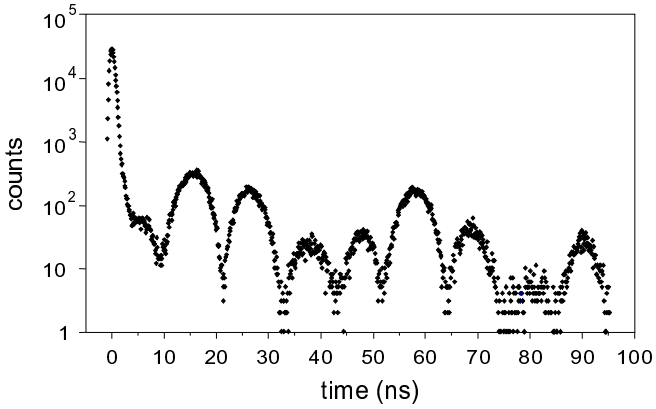

Figure 5.5: TDSRS spectrum of a magnetically split Fe sample ($T_{eff} = 21$) in the presence of a crossed polarizer and analyzer.

For comparison, the TDSRS spectrum is given in figure 5.5. This spectrum is taken under the same conditions, after having removed the stainless-steel reference sample. The forward-scattered intensity is now recorded versus time after excitation by the synchrotron pulse. The data collection time was 10 minutes with a resonant count rate of 55 photons/s. The beat pattern in the time-dependent spectrum reflects all hyperfine information since the quantum beats are determined by the energy differences in the sample [16, 17].

5.3 Discussion

5.3.1 Qualitative comparison between TISRS and TDSRS

TISRS and TDSRS yield the same hyperfine and solid-state information. The time differential synchrotron-radiation spectroscopy is obviously more suited in cases where time-dependent phenomena are to be studied, or if one is particularly interested in the dynamics of the system. If, on the other hand, hyperfine interactions are the object of the measurement, then time-integrated synchrotron-radiation spectroscopy can be considered as well. It has the advantage over TDSRS to yield spectra that are easier to interpret. This becomes a real advantage when samples with many hyperfine components are studied. The TISRS spectrum is just a superposition of spectra, each one belonging to a component. In TDSRS, on the other hand, all components interfere, so that each pair of transition frequencies produces a quantum beat. The number of quantum beats can become very large, resulting in a complicated beat structure. Extensive computer packages, such as CONUSS [65], MOTIV, NERT and EFFINO [66], are used to extract the hyperfine information from the TDSRS spectra.

An important difference between TISRS and TDSRS with crossed polarizer/analyzer concerns the data collection time. The spectra from figures 5.4 and 5.5 were recorded with comparable resonant count rates, yet for TISRS it took 30 times longer to get a good spectrum. This can be explained as follows. In case of TDSRS, the signal is formed by radiation resonantly scattered on the investigated sample. Since this radiation is the only one passing through the analyzer, one measures 100% signal. See figure 5.6.
For TISRS, there are two processes that contribute to the spectrum. The first one, the most intense, is radiation resonantly scattered by the investigated sample, without being scattered by the reference sample. This process has no velocity dependence and hence, it will only contribute to a constant background. The actual signal is formed by radiation that has been resonantly scattered both on the sample and on the reference. However, this is a double-scattering event. The extra scattering on the reference makes it a less likely process than the single scattering on the sample only. As a consequence, the signal-to-background ratio is decreased by a certain factor, depending on the effective thicknesses of the samples. In order to get comparable statistics as in TDSRS, the measuring time will be enlarged by the inverse square of this factor.

Additionally, there is another effect to account for. Data collection times will also be longer for TISRS due to the fact that counts are measured sequentially over the velocity scale. As in conventional Mössbauer spec-

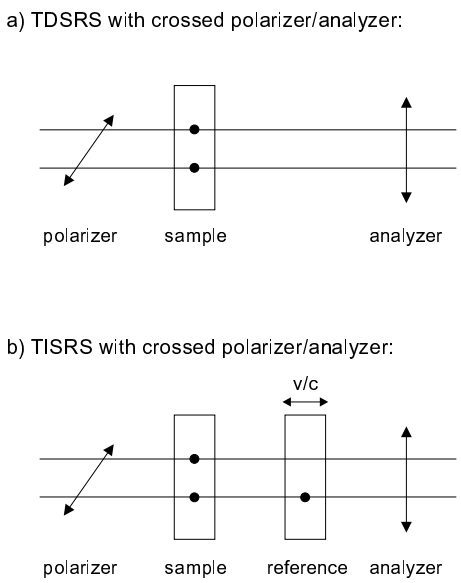

Figure 5.6: Comparison between TDSRS and TISRS when a crossed polarizer and analyzer are used.

troscopy, channels corresponding to the baseline (off-resonance channels) yield no information on the hyperfine parameters. Since these channels are also considered, the statistics will be reduced to some extent. This effect accounts for an additional factor two or three difference in data collection time.

In a conventional TISRS measurement (without polarizer and analyzer) only the last argument remains. The detected intensity is an interference between two single-scattering paths, just as in TDSRS. This is shown schematically in figure 5.7. In that configuration, the data collection times for the two methods only differ by a factor of two or three.

5.3.2 Use of polarizer and analyzer in TISRS

Although the implementation of the polarizer and analyzer filters reduces the undesired prompt radiation, it limits the possible applications. In order to change the polarization state of the radiation, samples with a uniquely defined orientation of the hyperfine field are required (cf. chapter 3). This is a minor disadvantage when purely magnetic systems are studied, but requires monocrystals if a quadrupole interaction is involved. Furthermore, the study of single-line samples with this setup is simply excluded.

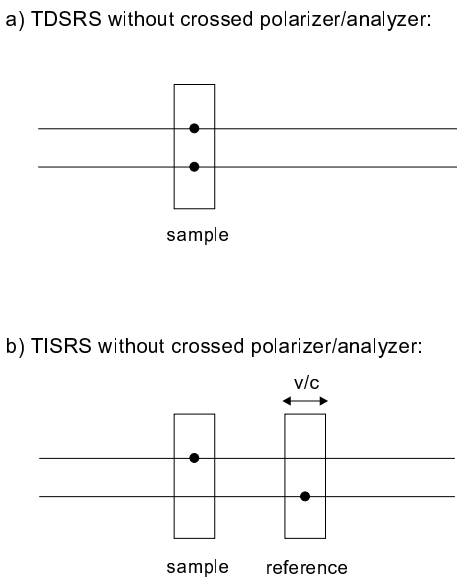

Figure 5.7: Comparison between TDSRS and TISRS when no crossed polarizer and analyzer are used.

Another drawback of using a polarizer and analyzer for TISRS is the low countrate. The resonant count rate was only 40 photons/s. This is two orders of magnitude smaller than in other nuclear resonant scattering experiments, where a high-energy-resolution monochromator is used to reduce the bandwidth of incoming radiation. This is an important factor when dealing with low resonant intensities. Data collection times of a few minutes (when no polarizer/analyzer is used) become several hours (with crossed polarizer/analyzer). If, however, the resonant intensity from the synchrotron can be increased by a factor of 100 or 1000, the data collection time will be a few seconds versus a few minutes. Then, in both cases, spectra with sufficient statistics are produced in a short time. Although the relative difference in data collection time would still be two or three orders of magnitude, this difference is not relevant anymore and the setup with crossed polarizer/analyzer becomes interesting for TISRS measurements.

With currently available resonant intensities, however, the use of a polarizer and analyzer for time-integrated synchrotron-radiation spectroscopy is unfavorable from a statistical point of view. In order to make TISRS more generally applicable for the study of hyperfine interactions, one needs to find an appropriate way to filter out nonresonant radiation to an extent that is tolerable by the detector, without losing too many statistics.

5.4 Conclusion

In this chapter a TISRS experiment is reported in which the prompt nonresonant radiation was substantially suppressed by the inclusion of a crossed polarizer and analyzer in the setup. Hence, the time gate could be minimized to a value acceptable for TISRS. The measurement gave nice spectra in energy domain, that could be reproduced by simulations for fully time-integrated synchrotron-radiation spectroscopy. The interpretation of the spectra is much easier than the equivalent time differential ones, and therefore, TISRS allows on-line decisions to be made. It is an adequate hyperfine technique, especially suited for the study of samples with many hyperfine levels.

The present experiment suffered from very low resonant count rates, and, consequently, from long measuring times. This is mainly due to the polarizer/analyzer setup. If TISRS is to become competitive with TDSRS, this problem has to be solved and other solutions need to be found to reduce the intensity of nonresonant radiation.

Chapter 6

Possible Improvements

In the previous chapters, it has been demonstrated that unperturbed TISRS spectra can only be obtained when the full time response of the targets is recorded. However, in practice, one has to put a gate in order to inhibit detection at the arrival of the synchrotron pulses. For the ^{57}Fe resonance, the acceptable time gate is ≈ 5 ns. This result was obtained in chapter 4 for single-line samples ($T_{\text{eff}} = 2 \times 9$). In the presence of hyperfine splitting of the nuclear levels, it is expected that this value will even be less ($\approx 1-3$ ns). This requirement cannot be fulfilled with the beam from a high-resolution monochromator. Therefore, a crossed polarizer and analyzer were included in the setup. The time gate could be pushed below the acceptable value. In the present chapter alternative solutions will be discussed.

As a first possibility, the use of a nuclear monochromator is investigated. If it were possible to reduce the bandwidth of incoming radiation to such an extend that the beam intensity is reduced to a level acceptable for the detector (and electronics), and simultaneously keep the bandwidth broad enough to excite all hyperfine levels, then time slicing could be avoided. It will be shown, however, that existing nuclear monochromators are not suited for application in TISRS because of their relatively slow time response.

Other solutions, like the development of an ultrafast shutter or an array of stacked detectors, are briefly explained. Both handle the problem of the high prompt intensity at the detector level itself.

Finally, the use of an X-ray interferometer in TISRS is discussed. The interferometer provides a possibility to suppress the prompt intensity almost completely, without altering the TISRS signal. The basic idea behind this setup will be explained and some preliminary simulations will be shown.

6.1 Nuclear Monochromator

Forward scattering experiments require a strong reduction of the energy bandwidth around resonance. The lower limit obtained by pure electronic monochromatization for X-rays in the 10 - 30 keV region is of the order of meV. Since nuclear level widths are typically of the order of neV, this still gives a ratio of nonresonant to resonant intensity of 10^6. For further suppression of the nonresonant radiation, nuclear monochromators should be used. Several nuclear monochromators have been suggested and tested, such as grazing incidence antireflection (GIAR) films, or single crystals with pure nuclear reflections (i.e., reflections that are electronically forbidden, but nuclearly allowed), and since recently, nuclear resonant multilayers. Below, a short explanation on these three types of nuclear monochromators is given. Later on, the possible application in TISRS will be discussed.

Grazing Incidence Antireflection Film

Grazing incidence antireflection films on a flat mirror have been proposed as broad band nuclear resonance filters for synchrotron radiation [67]. A GIAR film, in its most simple design, consists of a coating containing resonant nuclei, on a backing with higher electron density.
A profound theoretical description and detailed derivation of the properties of GIAR films, is given in a series of papers [68, 69, 70, 71].

The synchrotron radiation falls onto the film at a grazing angle, φ_{in}. Due to the difference in index of refraction for resonant and nonresonant radiation, the resonant radiation will be nearly totally reflected at the film surface, while the nonresonant radiation is strongly absorbed in the coating layer. See figure 6.1 for an illustration.

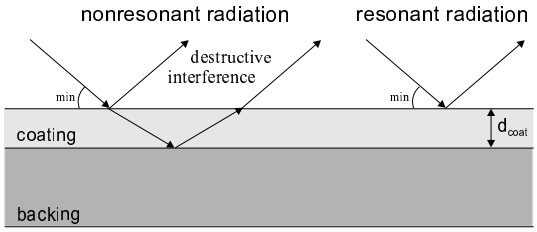

Figure 6.1: Scattering of synchrotron radiation by GIAR films. The resonant and the nonresonant radiation are artificially separated for reasons of clarity.

In the vicinity of the nuclear resonance, there is a large nuclear contribution to the index of refraction, n, which is connected to the critical angle φ_c via the formulae

$$n = 1 - \delta - i\beta$$
$$\varphi_c = \sqrt{2\delta}$$

For X-rays in the 10 keV range, typical values are $\delta = 10^{-5} - 10^{-6}$ and $\beta = 10^{-6} - 10^{-7}$. Thus, critical angles are in the range of a few mrad. The critical angle for total reflection is much larger for the resonant radiation than for the nonresonant one. There exists a region of angles of incidence φ_{in}, where the nonresonant radiation is deeply penetrating into the medium, but the resonant radiation is nearly totally reflected:

$$\varphi_c(\text{electr.}) < \varphi_{in} < \varphi_c(\text{nucl.})$$

For further suppression of the nonresonant radiation, the thickness of the coating, d_{coat}, is adjusted to yield destructive interference between the waves reflected at the layer boundaries. The backing material should have a higher electron density and, thus, a larger reflectivity than the coating layer in order to compensate the absorption of the beam going through the coating. As a result, the two outgoing waves can be made of equal amplitude and in antiphase, resulting in maximal destructive interference. At a certain angle of incidence, φ_{min}, a deep minimum in the nonresonant reflectivity occurs.

The degree of electronic suppression that can be reached with a GIAR film depends on the divergence of the incoming beam and the width of the minimum in the (electronic) rocking curve. At undulator sources, a suppression factor in the order of 10^{-3} can be achieved.

Pure Nuclear Reflection from a Single Crystal

Another possibility to obtain resonant radiation out of the white synchrotron beam is by using pure nuclear reflections. These occur in enriched antiferromagnetic single crystals, such as $^{57}FeBO_3$ [72, 73] or $^{57}Fe_2O_3$ [74]. Due to the symmetry breaking antiferromagnetic hyperfine interactions, the nuclear periodicity is twice as large as the electronic periodicity, resulting in pure nuclear reflections at selected Bragg angles. For the theory of nuclear resonance diffraction the reader is referred to Refs. [49, 75, 76].

In figure 6.2 the crystalline structure of $FeBO_3$ is shown. The primitive unit cell is a rhombohedron, containing two molecules of the material. The Fe ions are positioned at the origin and the center of the [1 1 1] diagonal. At room temperature, $FeBO_3$ is an antiferromagnet. The two magnetic sublattices have equal magnetic moments, but with opposite orientation. The nuclear scattering is sensitive to the magnetic moments, and hence, the two sublattices are inequivalent. The periodicity is determined by Fe layers

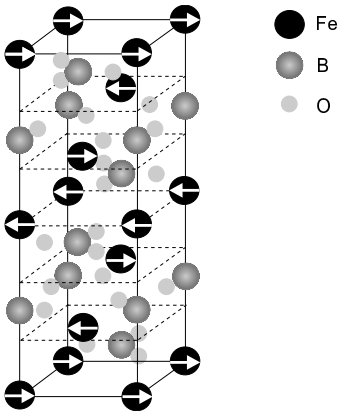

Figure 6.2: Conventional unit cell of $^{57}FeBO_3$. The dashed lines define the planes containing Fe nuclei with the same direction of the magnetic moments.

with collinear magnetic moments. For electronic scattering, on the other hand, no distinction can be made between the two magnetic sublattices and the periodicity is half of the nuclear periodicity. As a consequence, the Bragg peaks for resonant and for nonresonant radiation appear at different angles. For certain Bragg reflections the nuclear reflectivity is high, while the electronic scattering is suppressed.
Due to strong interference between the hyperfine components and due to broadening of the resonance lines up to 30 Γ_0, $^{57}FeBO_3$ can be effectively used as a broad band filter for synchrotron radiation. Nuclear reflectivities of more than 40 % have been reported [77] and the region of high reflectivity extends over 120 Γ (≈ 0.6 μeV).

An important limitation for the use of single crystals with pure nuclear reflections as monochromators for synchrotron radiation is the ability to produce a perfect single-crystal that is maximally enriched in the Mössbauer isotope.

Nuclear Resonant Multilayers

Pure nuclear reflections from single crystals require a magnetic crystal structure, and hence, hyperfine splitting of the nuclear levels. This yields a complicated energy structure of the scattered beam which is unfavorable for nuclear resonance scattering experiments.

Artificially layered structures were recently proposed for pure nuclear diffraction of synchrotron radiation. They can be prepared without magnetic hyperfine splitting, by selecting an appropriate surrounding for the resonant

isotope. Moreover, they leave a wide choice of elements so that it is possible to develop a resonant multilayer for various isotopes. Another attractive feature of synthetic multilayers is that it is possible to arrange a large interlayer distance in the superlattice, an thus, to achieve small diffraction angles, resulting in wide nuclear rocking curves. The angular acceptance of a nuclear resonant multilayer can easily be made larger than the divergence of synchrotron radiation beams.

Nuclear multilayers are artificially layered structures involving alternating layers of differing isotopes, creating a nuclear periodicity different from the electronic periodicity.

An example of an artificial multilayer, that was proposed for the filtering of synchrotron radiation at the ^{57}Fe resonance [78, 79], is [^{57}Fe(22)/Sc(11)/ Fe(22)/Sc(11)] $\times$ 25 [1]. The intermediate layer between two Fe layers prevents the interdiffusion of ^{57}Fe and Fe into each other. Sc is chosen to obtain a single-line structure of the nuclear levels of ^{57}Fe as a result of partial diffusion of Sc into the Fe layers. The thickness of all Fe layers is equal, so that the nuclear periodicity (determined by the ^{57}Fe layers) is twice the electronic periodicity (determined by all Fe layers). As a consequence, the first order Bragg peak for the resonant radiation will appear at nearly half the Bragg angle for the nonresonant radiation. This is nothing but the translation of Bragg's law:

$$2\, d\, sin\theta = n\, \lambda \qquad \begin{array}{l} (n = 1, 2, 3, \ldots \text{ for constructive interference}) \\ (n = \frac{1}{2}, \frac{3}{2}, \frac{5}{2}, \ldots \text{ for destructive interference}) \end{array}$$

where $sin\theta$ can be approached by θ for small angles of incident radiation. d is the interplanar distance.
For odd order nuclear Bragg angles, the resonantly scattered radiation fulfills the condition for constructive interference, while the nonresonant radiation will interfere destructively. This way, pure nuclear diffraction of γ-radiation is obtained. The electronic reflectivity at the nuclear Bragg angle is only 10^{-3}.

Another example of a resonant multilayer is [^{57}Fe(17)/Cr(10)] $\times$ 25. In this system, the thickness of the Cr layers is chosen such as to exhibit antiferromagnetic coupling in the ^{57}Fe layers. Therefore, the magnetic periodicity of the multilayer is twice the electronic periodicity, resulting again in pure nuclear Bragg reflections [80]. Here, the electronic suppression is 3×10^{-4}.

The performance of a nuclear multilayer is determined by the optical constants of the layer materials, the number of bilayers and the thickness ratio of the layers within a bilayer.

[1] The standard notation for multilayers has been adopted: $[A(d_A)/B(d_B)] \times N$, meaning that the structure contains N layers of element A and B, with respective thickness d_A and d_B, expressed in Å.

6.1.1 Application of a Nuclear Monochromator in TISRS

A nuclear monochromator could be used in TISRS to reduce the nonresonant intensity that causes the overload of the detector system [81].
Suppose a nuclear monochromator is placed after the high-resolution monochromator, up-stream with respect to the sample and reference targets (see figure 6.3). A large portion of the nonresonant radiation will be suppressed by the nuclear monochromator and only a small bandwidth around resonance will be reflected. Typical energy bandpasses are in the range of 0.5 μeV [77, 82], corresponding to count rates of $\approx 5 \cdot 10^5$ Hz. This value is below the detector limit and would allow to perform fully time-integrated measurements.
The aim of the present section is to analyze the usefulness for TISRS of further monochromatization of the synchrotron beam by means of a nuclear monochromator [83]. In the following discussion the nuclear monochromator has been assumed to be a single crystal with pure nuclear reflections. A similar reasoning holds for GIAR films and nuclear resonant multilayers.

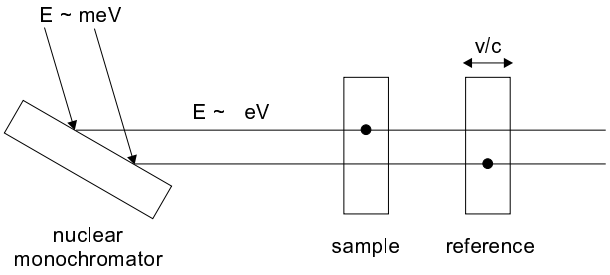

Figure 6.3: Scheme of TISRS with nuclear monochromator.

If a nuclear monochromator is included in the setup for TISRS, as in figure 6.3, then expression (3.10) from chapter 3 for the transmitted wavefields after the sample and reference should be replaced by:

$$\begin{bmatrix} A^x_{tr}(\omega) \\ \\ A^y_{tr}(\omega) \end{bmatrix} = U^{-1}\, R\, S\, U\, M \begin{bmatrix} A^x_{in}(\omega) \\ \\ A^y_{in}(\omega) \end{bmatrix}$$

where $A^x_{in}(\omega)$ and $A^y_{in}(\omega)$ are the wavefields incident on the nuclear monochromator. M is a 2×2 matrix describing the response of the monochromator.

Consider the example of a thick single-line nuclear monochromator for ^{57}Fe with symmetric Bragg reflection. The reflectivity relief looks like figure 6.4. Far off the nuclear Bragg angle, the reflectivity is sharply peaked around resonance. Vice versa, far off resonance energy, the reflectivity curve is sharply peaked around the exact Bragg angle. In the vicinity of the nuclear resonance and the Bragg angle, the reflectivity profile is very much broadened. This is easily seen from the two cross-sections shown in figure 6.4.

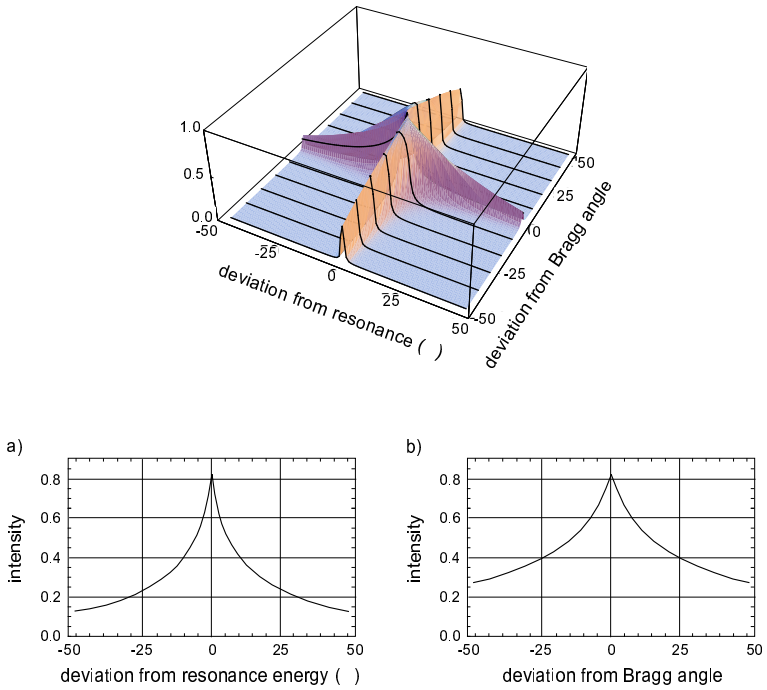

Figure 6.4: Top: Typical reflectivity relief of a single-line nuclear monochromator for the ^{57}Fe resonance, with symmetric Bragg reflection. Below: cross-sections of the reflectivity profile at exact Bragg angle (a); and at exact resonance energy (b).

The most important property for the application of nuclear monochromators in TISRS is the fact that the nuclear reflectivity is not constant around resonance. For the example considered, although the region of high reflectivity at the exact Bragg angle extends over 100 natural linewidths, it has a peak around resonance and falls off with increasing energy deviation. As a consequence, the broadband excitation of sample and reference is not

uniform as a function of energy. The excitation of the reference sample will vary as it scans over the energy region. Therefore, the baseline in the TISRS spectrum will no longer be constant. This is illustrated for the nuclear monochromator under consideration in figure 6.5.
If a nuclear monochromator with pure nuclear reflections is used, such as $^{57}FeBO_3$, the nuclear reflectivity profile will show even more structure due to the hyperfine splitting of the resonance and the time-integrated spectrum will look even more complicated.

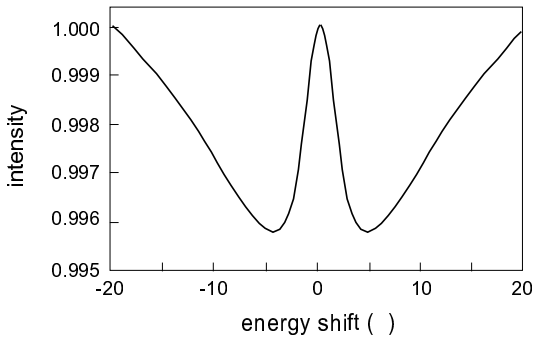

Figure 6.5: Simulated TISRS spectrum with a single-line nuclear monochromator included in the setup. The sample and reference are both single-line absorbers with effective thickness $T_{eff} = 10$.

The energy structure of the nuclear monochromator can be excluded from the TISRS spectrum by cutting off the response of the monochromator in time. For a thick monochromator, the time response is very short due to speedup, providing a very short excitation signal for the samples, which will deexcite with some delay according to the nuclear lifetime. If a time window is selected that starts after the nuclear monochromator response has died out, then only delayed radiation scattered from the samples is recorded. The structure of the nuclear monochromator will not be present anymore in the TISRS spectrum.
But, inspecting the time response of a single-line nuclear monochromator with a bandpass of 100 Γ, it is found that the excitation signal has a tail which extends over several tens of ns. (See figure 6.6.) The contribution of the nuclear monochromator is mainly excluded when 30 ns are cut off. This time interval exceeds the permitted one for TISRS by one order of magnitude. As has been shown before, such a big truncation of the scattered intensity distorts the spectra significantly.

For the purpose of TISRS one needs a monochromator whose response is appreciably enhanced due to speedup (time response enclosed within 3 ns). However, such a monochromator does not yet exist.

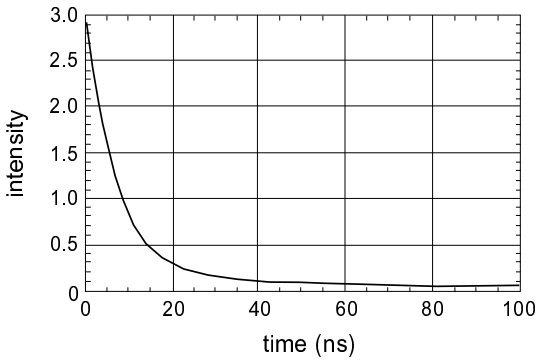

Figure 6.6: Evolution of the scattering at exact Bragg angle from a single-line nuclear monochromator having a bandpass of 100 Γ.

6.1.2 Conclusion

If a nuclear monochromator is used ($\Delta E \approx 0.5$ μeV, intensity $\approx 5 \cdot 10^5$ Hz), the detection problem is practically solved. However, the nuclear monochromator will have a delayed response for about 30 ns. If this response is included in TISRS, the spectra are modified by the structure of the nuclear monochromator. If excluded, the large time gate will introduce distortion of the TISRS spectrum, just like the experimental results described in chapter 4.

For the application in TISRS, the nuclear monochromator should satisfy the following requirements:

1. The energy bandpass has to be broader than the hyperfine splitting of the sample, so that all nuclear transitions are excited coherently.
2. On the other hand, the bandpass should be small compared to the spectrum of incident radiation, so that the detector is not overloaded by the prompt pulse.
3. The time response should be very short without a tail at long times.

A nuclear monochromator with a bandpass of 1 - 5 μeV fulfills these three conditions. The time response would be less than 5 ns and the count rate approximately 10^6 Hz, which is quite tolerable for the detector. However, such a monochromator exceeds the bandpass of existing monochromators by one order of magnitude. To date, there is no idea how such a large bandwidth could be realized.

6.2 Ultrafast Shutter

A principle solution to the problem of the high prompt intensity is to create an ultrafast shutter. With an ultrafast shutter in front of the detector it would be possible to close the shutter for a very short time ($\approx$ 1 ns) at the arrival of the synchrotron pulses and to open it again in the intermediate interval. This way, the detector does not get the overwhelming prompt intensities, but only the delayed intensity which is several orders of magnitude weaker.

One can think of a perfect single crystal where the electronic Bragg reflection is suppressed by a sudden change in the interplanar distance. In Ref. [84] it is shown that efficient Bragg reflection can be switched on and off by illumination with ultrafast laser pulses. When the repetition rate of the laser pulse is synchronized to that of the synchrotron pulses, the direct intensity will be blocked, while the delayed radiation is transmitted through the crystal.

In Ref. [85] the use of a time gate quartz device as ultrafast shutter is reported. The basic idea is to use a quartz resonator crystal with the same frequency as the synchrotron pulse repetition rate. The displacement of the diffraction planes varies as a function of the applied field. According to Bragg's law, this results in a shift of the diffraction angle. When synchronizing the resonator function generator with the synchrotron rf-trigger, this quartz device could be used as an ultrafast shutter for synchrotron pulses, provided one can enlarge the bandwidth of the signal so that all hyperfine components are enclosed, while maintaining a constant resonator frequency.

6.3 Stacked Detectors

Another proposal is to use an array of very thin, stacked detectors. The energy deposit would be smeared out over several detectors. Due to their small lateral dimensions, each detector sees only part of the incoming intensity and cannot get overloaded. On the other hand, by putting many such detectors one after the other, the total efficiency of the system remains high. However, this idea is not even in the design stage.

6.4 X-ray Interferometer

An elegant method to suppress the nonresonant radiation is to use an X-ray interferometer in combination with a π-phase shifter. The interference of two beams in an X-ray interferometer has been demonstrated in Refs. [86, 87, 88]. A symmetric triple Laue interferometer was used which is made of a silicon single crystal. Figure 6.7 shows a schematic picture.

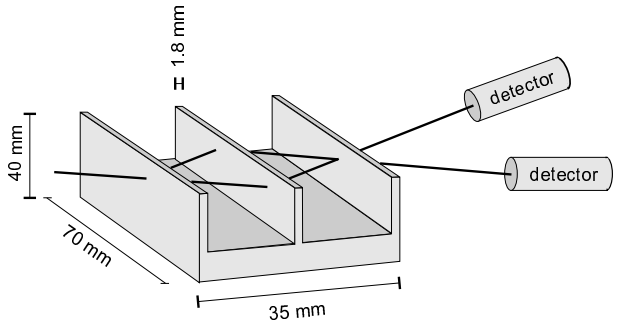

Figure 6.7: Scheme of the triple Laue interferometer [89].

The incident X-ray beam is split into two coherent ones at the first plate of the interferometer. Each of them is reflected by the second plate. The reflected beams are recombined at the third plate and two beams leave the interferometer. Only the outgoing beam parallel to the incident one will be considered here.

The interferometer can be oriented in such a way that the σ-polarization vector of the electric field lies in the crystal planes of the interferometer. In this case the polarization is not changed after Laue diffraction.

Figure 6.8 shows the setup for TISRS with X-ray interferometer. The first plate of the interferometer splits the incident beam into two coherent paths. In one path a phase shifter of 180° is placed as well as a moving single-line absorber. This is the reference sample for TISRS. The other path contains the sample under investigation.

The Laue diffraction of the synchrotron radiation by each plate of the interferometer can be described by the reflection and transmission matrices, R_i and T_i, defined in a base of linear polarization:

$$\text{plate i}: \quad R_i = \begin{bmatrix} r_i & 0 \\ 0 & r_i' \end{bmatrix} \qquad T_i = \begin{bmatrix} t_i & 0 \\ 0 & t_i' \end{bmatrix}$$

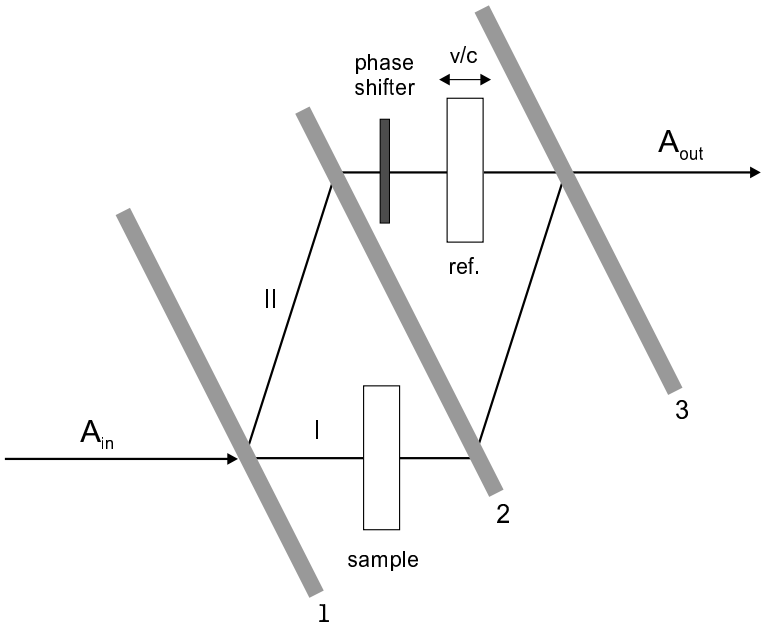

Figure 6.8: Schematic view of the setup for TISRS with X-ray interferometer.

Because of the orientation of the interferometer, no polarization mixing occurs and, hence, all off-diagonal elements are zero. For this application, the first and last plates of the interferometer should be identical, so that $R_3 = R_1$ and $T_3 = T_1$.

The action of the π-phase shifter can be described by

$$Ph = -\begin{bmatrix} 1 & 0 \\ 0 & 1 \end{bmatrix}$$

Finally, the transmission of radiation through the reference and investigated sample is given by the matrices R and S', respectively, with

$$S' = U^{-1}\,S\,U = \begin{bmatrix} A' & B' \\ C' & D' \end{bmatrix}$$

An explicit expression for the matrix elements A', B', C' and D' can be calculated by means of the definitions for the matrices U^{-1}, U and S in chapter 3. R is a diagonal matrix given by Eq. (3.8).

With these notations, the amplitudes of outgoing radiation for both paths in the interferometer can be calculated easily.

$$A^{I}_{out}(\omega) = R_3\ R_2\ S'\ T_1\ A_{in}(\omega) \tag{6.1}$$

$$A^{II}_{out}(\omega) = T_3\ R\ Ph\ R_2\ R_1\ A_{in}(\omega) \tag{6.2}$$

The superscripts refer to path I and path II. The total amplitude for radiation leaving the interferometer is the coherent sum of the amplitudes resulting from the different paths.

$$\begin{aligned} A_{out}(\omega) &= A^{I}_{out}(\omega) + A^{II}_{out}(\omega) \\ &= (R_3\ R_2\ S'\ T_1 + T_3\ R\ Ph\ R_2\ R_1)\ A_{in}(\omega) \end{aligned} \tag{6.3}$$

From Eq. (6.3) the total intensity in the detector can be calculated according to

$$I_{out}(v) = \frac{1}{2\pi} \int_{-\infty}^{+\infty} d\omega\ |A_{out}(\omega)|^2$$

6.4.1 Single-line Sample

If the investigated sample is a single-line absorber, then $S' = S$ reduces to a diagonal matrix and the formulae (6.1) and (6.2) take a very simple form

$$A^{I}_{out}(\omega) = +\ r_1\ r_2\ t_1\ S\ A_{in}(\omega)$$

$$A^{II}_{out}(\omega) = -\ r_1\ r_2\ t_1\ R\ A_{in}(\omega)$$

The total amplitude for outgoing radiation becomes:

$$A_{out}(\omega) = r_1\ r_2\ t_1\ (S - R)\ A_{in}(\omega) \tag{6.4}$$

The amplitude of radiation transmitted through an absorber consists of two parts (cf. Eq. (3.5)):

$A_{in}(\omega)$: the incident radiation corresponding to transmission without interaction
$A_{sc}(\omega)$: radiation coherently scattered in forward direction

Thus, one can write

$$S\,A_{in}(\omega) = A_{in}(\omega) + A_{sc}^{S}(\omega)$$

$$R\,A_{in}(\omega) = A_{in}(\omega) + A_{sc}^{R}(\omega)$$

Here, the superscripts S and R refer to the sample an the reference, respectively. Substituting these expressions in Eq. (6.4) yields

$$A_{out}(\omega) = r_1\,r_2\,t_1\,\left(A_{sc}^{S}(\omega) - A_{sc}^{R}(\omega)\right)$$

The detected intensity for a single-line sample now becomes

$$I_{out}(v) = \frac{r_1^2\,r_2^2\,t_1^2}{2\pi}\int_{-\infty}^{+\infty} d\omega\,\left\{\left|A_{sc}^{S}(\omega)\right|^2 + \left|A_{sc}^{R}(\omega)\right|^2 - 2\,Re\left(A_{sc}^{S}(\omega)\,A_{sc}^{R*}(\omega)\right)\right\} \qquad (6.5)$$

When the intensity is recorded as a function of the reference's velocity, the first two terms in the integral will contribute to the background while the interference term $2\,Re\left(A_{sc}^{S}(\omega)\,A_{sc}^{R*}(\omega)\right)$ will contribute to the signal, containing all hyperfine information.

In Eq. (6.5) the amplitude of the incoming radiation does not appear. In other words, the highly intense prompt radiation is not detected. It has been suppressed by the relative phase shift of 180° between both paths in the interferometer. The detector registers only resonant radiation that has interacted with the samples.

Figure 6.9 shows a simulated spectrum for TISRS with X-ray interferometer in case of a single-line sample. The detected intensity has been normalized according to

$$I_{\mathrm{norm}}(v) = \frac{1}{N\,r_1^2\,r_2^2\,t_1^2}\,\frac{I_{out}}{I_{in}}$$

with N the number of velocity channels.

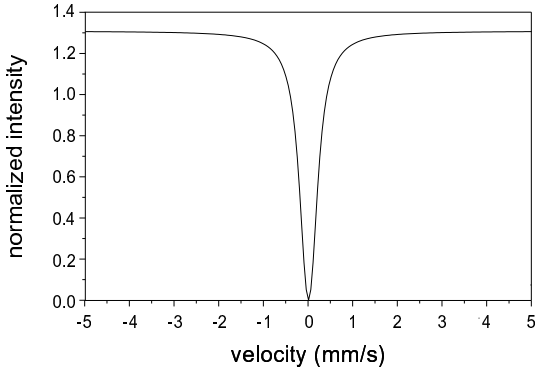

Figure 6.9: Simulation for TISRS with X-ray interferometer. The sample and the reference are both stainless-steel absorbers with an effective thickness $T_{eff} = 5$.

6.4.2 Sample Submitted to Hyperfine Interaction

If the investigated sample is submitted to a hyperfine field in a well defined direction, then the transmission of X-rays through the sample will introduce polarization mixing. The outgoing amplitude after the interferometer will contain two orthogonal polarization components.

The outgoing amplitudes for both paths can be written as

$$A^{I}_{out}(\omega) = A^{I\sigma}_{out}(\omega) + A^{I\pi}_{out}(\omega)$$

$$A^{II}_{out}(\omega) = A^{II\sigma}_{out}(\omega)$$

The outgoing amplitude of path II only contains a σ-polarization component because the reference is a single-line and cannot change the polarization state of the radiation.

The resulting intensity is given by

$$I_{out}(v) = \frac{1}{2\pi} \int_{-\infty}^{+\infty} d\omega \left\{ \left| A^{I\sigma}_{out}(\omega) + A^{II\sigma}_{out}(\omega) \right|^2 + \left| A^{I\pi}_{out}(\omega) \right|^2 \right\}$$

Only the σ-component contains an interference between the sample and

the reference. The π-component is independent of the reference's velocity and will only give rise to an additional background contribution.

In figure 6.10 a simulation for a magnetically split ^{57}Fe sample is displayed. The background from radiation with π-polarization has been subtracted.

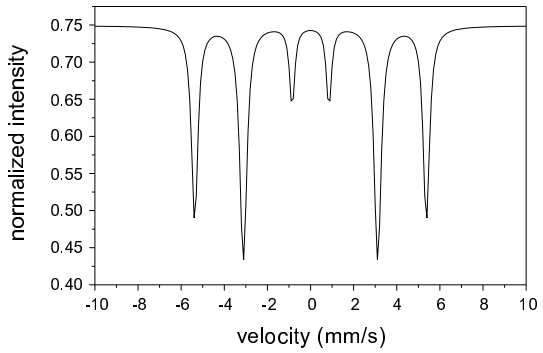

Figure 6.10: Simulation for TISRS with X-ray interferometer for a ^{57}Fe absorber with effective thickness $T_{eff} = 10$ and a stainless-steel reference absorber with effective thickness $T_{eff} = 2$. The ^{57}Fe absorber is submitted to a hyperfine magnetic field B = 33 T, oriented perpendicular to the beam direction and under an angle of 45° with respect to the polarization plane of the synchrotron.

6.4.3 Conclusion

Simulations have shown that the combined application of an X-ray interferometer and a π-phase shifter in TISRS suppresses the prompt nonresonant intensity. However, the description presented above is a simplified picture because the attenuation of the wave field by transmission through the phase shifter has been neglected. Moreover, since the incoming synchrotron radiation has a broad spectrum, the frequency dependence of the phase shift should be taken into account. Both arguments will yield an incomplete suppression of the prompt radiation. A small time gate will be required in order to reduce the background of nonresonant radiation. More profound research needs to be done, including an estimation of the prompt suppression and of the resonant count rates that can be expected.

Chapter 7

Conclusions

In this thesis work a new, time-integrated technique for nuclear resonant forward scattering experiments with synchrotron radiation has been developed. Two experiments with TISRS were carried out which show the feasibility and usefulness of the method. When crossed polarizer and analyzer crystals are included in the setup, the prompt nonresonant radiation can be sufficiently reduced and TISRS can be performed without time gate. The main advantage of TISRS is that it is less dependent on the time mode of the synchrotron machine. TISRS can be a useful technique to study hyperfine interactions, especially in cases where time differential synchrotron radiation spectroscopy and classical Mössbauer spectroscopy are not straightforward. Typical examples are ^{181}Ta and ^{73}Ge.
The study of ^{181}Ta with TDSRS is extremely difficult because of the long lifetime of the excited state ($\tau = 8.73$ μs). Measuring a time spectrum, as was done by Chumakov [22], is only possible under extreme conditions: the storage ring should be operated in a single-bunch timing mode. But even then, the time interval between pulses was only 780 ns [22], which is not even one tenth of the natural nuclear lifetime. As a consequence, one needs samples with a large effective thickness so that the effective nuclear lifetime of the excited state is sufficiently decreased due to speedup and the nuclear decay can be measured during the time window. For this isotope, TISRS is a good alternative. It can be performed in a more efficient timing mode (a pulse separation of $\pm$20 ns) and will provide reliable hyperfine information. Another example is ^{73}Ge. It also has a long lifetime of the excited state ($\tau = 4.26$ μs), what complicates TDSRS for the study of hyperfine interactions. On the other hand, classical Mössbauer experiments are not possible because there is no source available. Again, time-integrated synchrotron-radiation spectroscopy could be a solution.

The most interesting application of TISRS, however, can be found in the study of very small hyperfine splittings in nuclei with a long lifetime of the excited state. If the hyperfine splittings are less than 0.1 neV, the corresponding quantum beat period becomes larger than 2 μs. Time windows available at the present synchrotron radiation storage rings are too short to follow such a slow quantum beat pattern and hence, most hyperfine information is not accessible by TDSRS. With the time-integrated method, on the other hand, these hyperfine splittings can be observed if the linewidth is small so that the different resonance lines in the spectrum are still resolved.

TISRS is also useful for giving additional information in TDSRS measurements. For instance, if time dependent phenomena are studied, knowledge of the energy spectrum is very useful for the analysis of the sometimes very complicated time spectra.

Since TISRS does not require a special mode of operation, it can, in principle, be applied in parasitic beam. This would considerably enlarge the time available for nuclear resonant scattering experiments and the number of experiments per year.

The new time-integrated method for nuclear resonant scattering experiments with synchrotron radiation is believed to be an important contribution to the field of hyperfine interaction techniques, which will become more and more attractive as the intensity at synchrotron radiation facilities increases.